Computational material design for acoustic cloaking

C. Méndez[1], J.M. Podestá[2], O. Lloberas-Valls[3,4],
S. Toro[2], A.E. Huespe[2,3]*, J. Oliver[3,4]

[1]CIMNE-Latinoamérica, Iturraspe 785, CP 3000, Santa Fe, Argentina

[2]CIMEC-UNL-CONICET, Predio Conicet Dr Alberto Cassano, CP 3000 Santa Fe, Argentina

[3]Centre Internacional de Metodes Numerics en Enyinyeria (CIMNE),Campus Nord UPC.

[4]E.T.S dEnginyers de Camins, Canals i Ports, Technical University of Catalonia (Barcelona Tech)

Campus Nord UPC, Mòdul C-1, c/ Jordi Girona 1-3, 08034, Barcelona, Spain

Abstract

A topology optimization technique based on the topological derivative and the level set function is utilized to design/synthesize the micro-structure of a pentamode material for an acoustic cloaking device.

The technique provides a micro-structure consisting of a honeycomb lattice composed of needle-like and joint members. The resulting metamaterial shows a highly anisotropic elastic response with effective properties displaying a ratio between bulk and shear moduli of almost 3 orders of magnitude. Furthermore, in accordance with previous works in the literature, it can be asserted that this kind of micro-structure can be realistically fabricated.

The adoption of a topology optimization technique as a tool for the inverse design of metamaterials with applications to acoustic cloaking problems is one contribution of this paper. However, the most important achievement refers to the analysis and discussion revealing the key role of the external shape of the prescribed domain where the optimization problem is posed.

The efficiency of the designed micro-structure is measured by comparing the scattering wave fields generated by acoustic plane waves impinging on bare and cloaked bodies.

---

*Corresponding author. E-mail address: ahuespe@intec.unl.edu.ar (A.E. Huespe).

1 Introduction

New methodologies to fabricate metamaterials open a wide range of interesting applications in engineering and science. In this context, the goal is to design and manipulate architectured micro-structures to develop new materials with exotic mechanical, optical, acoustical or thermal properties (Zheng et al. [1], Kadic et al. [2], Narayana and Sato [3]). These metamaterials are envisaged to satisfy specifically given requirements at the macro-structure scale level.

For example, making an object *invisible* to sound waves can be achieved by covering it with an appropriately designed layer of material having extreme and highly anisotropic elastic properties. Following this kind of approach, one technique to get acoustic cloaking is based on the coordinate transformation method, reported by Norris [4], whereby the material properties of the cloak copy the geometrical coefficients of an adequate space (singular) transformation. Norris has generalized the key observation of Pendry et al. [5] to acoustic wave problems. Pendry has shown that metamaterials can be designed at will, by adopting singular coordinate transformations, to redirect electromagnetic waves and, therefore, attaining optical cloaking devices.

According to Norris, metamaterials for cloaking systems based on transformation acoustic can be categorized into two broad classes: materials requiring anisotropic inertial mass densities, identified with inertial cloaking devices (see Cheng et al. [6] for realizations of this type of metamaterial), and materials requiring anisotropic bulk moduli. Realizations of this last type of metamaterials can be reached through pentamode materials.

Pentamode materials have been initially proposed by Milton and Cherkaev ([7]). These materials are usually formed by truncated cones, similar to bars, and joints which are spatially distributed as a Bravais lattice.

Layman et al. [8] have developed a design methodology for pentamode materials employed in acoustic cloaking devices. In their approach, these authors use a methodology where the micro-structure topology is prescribed beforehand, i.e. the micro-structure has a pre-defined architecture. The dimensions and geometrical position of each member constituting the micro-structure are parametrized. The most convenient set of parameters is then determined through a non-linear programming algorithm, such that the effective elastic properties are adjusted to those values required by Norris's analysis.

Additionally, pentamode materials have been fabricated and reported by Kadic et al. [9]. A number of issues concerning the material processing are addressed in [9]. An important conclusion reported in this paper, closely connected with the present work, is that in order to allow genuine pentamode material realizations, the members constituting the micro-structure have to be neither pin-jointed nor rigid-jointed.

The main objective of the present paper is to contribute to computational de-

sign/synthesis of pentamode material, constituted by highly heterogeneous microstructures, aiming to built acoustic cloaking devices. The question that has to be solved is how to distribute and combine the material within a prescribed domain to obtain the desired properties of the composite for building the cloaking device.

To solve this inverse design problem, we use a technique based on a topology optimization algorithm. Starting from the seminal paper of Bendsøe and Kikuchi [10] on topology optimization, there have been a huge number of well-known and established inverse techniques for material micro-structure design based on topology optimization. The book of Bendsoe and Sigmund [11] and, more recently, the review paper by Sigmund et al.[12] give excellent overviews of different approaches that can be found in the literature. Furthermore, a more specific discussion of topics here addressed can be found in the recent review by Osanov and Guest [13] and the references cited therein. It is important to mention that these kind of techniques provide a detailed description of the material micro-structure without preconceiving beforehand any kind of micro-architecture.

In this work, we adopt the topology optimization algorithm previously presented by Amstutz and Andrä [14], which uses a level set function and the topological derivative concept. This algorithm has been enhanced in posterior contributions of Amstutz and co-authors and successfully applied to a series of topology optimization problems, such as micro-structure inverse design ([15]), structural design subjected to stress constraints ([16]) and design of piezoelectric actuators ([17]). Furthermore, based on the contributions of Novotny and Sokołowski [18], who have obtained expressions of topological derivatives in the three-dimensional space, this kind of algorithm can be extended to solve 3D topology optimization problems. Synthesis of 3D micro-structures utilizing topological derivatives has been shown by Özdemir [19].

The Amstutz's algorithm is here adapted to seek the micro-structure topology of a material which effective elasticity tensor is equal to the target tensor given by Norris's analysis. It is shown that the Amstutz's algorithm, with some minor modifications introduced in the present contribution, turns to be an adequate technique for designing pentamode materials for acoustic cloaking.

Also, we analyze an important aspect of topology optimization techniques for designing metamaterials, which has not been particularly discussed in the literature. It refers to the relationship between the symmetry of the material to be synthesized and the external shape of the prescribed domain where the optimization problem is posed. Our results demonstrate that the external shape plays an important role in obtaining good micro-architecture designs. We propose a procedure to appropriately define this external shape. Conclusions extracted from this discussion can be extended to more general metamaterial inverse design problems using these techniques; provided that the effective properties of the target material satisfy given symmetry requirements. Discussion of this point is one of the main achievements of

3

the present paper.

A brief description of the topics covered in this paper is the following. First, in Section 2, some pentamode material properties are highlighted. These properties are subsequently utilized in the context of Norris's method. A reminder of this method is briefly presented in Appendix A. Also, in the same Appendix, the elasticity tensors reported by Gokhale et al. [20] are described and briefly summarized in sub-Section 2.1. They are the target tensors adopted in this work for the pentamode material inverse design.

In Section 3, a sketch of the topology optimization problem utilized for the micro-structure synthesis of the acoustic cloaking device is presented. A more detailed description of this procedure is shown in Appendix B.

The topology optimization algorithm described in Appendix B.3 is validated in sub-Section 3.3. The validation test consists of synthesizing an extremal metamaterial having a high ratio between the bulk and shear moduli.

The procedure for designing the micro-structure of the acoustic device is addressed in Section 4. The so-designed micro-structure is virtually tested through computational simulation of the scattered wave field produced by means of a cloaked object immersed in a fluid. The result is compared with the field produced by the same bare object. This assessment is presented in Section 5.

Finally, in Section 6, some conclusions are addressed.

2   A pentamode material

A Pentamode material is a class of extremal material having five easy (compliant) modes of deformation in a three-dimensional space, and having only one non-easy (hard) mode of deformation. The elasticity tensor of this material has one non-null eigenvalue and five null eigenvalues (hence the name of pentamode given to this class of material). For example, a compressible inviscid fluid (ideal gas) is a pentamode material, where shear strains in any directions represent easy modes of deformations, while volumetric strains represent hard modes of deformation. Milton and Cherkaev [7] have coined the name of pentamode materials in the context of linear elasticity, see also [21] where additional properties of this type of materials are analyzed.

Pentamode materials are a special class of linear anisotropic elastic solids. They can be characterized through elasticity tensors represented by:

$$\hat{\boldsymbol{C}} = \kappa^{\star} \boldsymbol{S} \otimes \boldsymbol{S} \qquad ; \tag{1}$$

where $\kappa^{\star}$ is a pseudo-bulk modulus with the dimensions of stress and $\boldsymbol{S}$ is an adimensional symmetric second order tensor with norm not necessarily equal to one. As usual, the symbol $\otimes$ denotes the tensorial product.

Pentamode materials are useful for constructing acoustic cloaking devices. These devices require a particular heterogeneous distribution of properties characterized by $\kappa^\star$ and $\boldsymbol{S}$. In particular, for cylindrical acoustic cloaking devices, it can be considered a rotationally symmetric pattern of material properties in the plane (X_1, X_2), schematized in Figure 1-a [1] , where the tensor $\boldsymbol{S}$ could be defined in a rather general context by:

$$\boldsymbol{S} = \sqrt{\frac{\kappa_r}{\kappa^\star}}(\boldsymbol{e}_r \otimes \boldsymbol{e}_r) + \sqrt{\frac{\kappa_\theta}{\kappa^\star}}(\boldsymbol{e}_\theta \otimes \boldsymbol{e}_\theta); \tag{2}$$

$\boldsymbol{e}_r$ and $\boldsymbol{e}_\theta$ being the radial and circumferential unit vectors related to the polar coordinate system. The material properties, $\kappa_r(\boldsymbol{X})$ and $\kappa_\theta(\boldsymbol{X})$ are seen as the radial and circumferential bulk moduli, respectively. Additionally, $\boldsymbol{S}$ satisfies a self-equilibrium condition: $\mathrm{div}_{\boldsymbol{X}}\boldsymbol{S} = \boldsymbol{0}$ [2] (note, however, that $\boldsymbol{S}$ is not a stress).

By adopting Voigt [3] notation for describing tensors of second and fourth order in the coordinate system defined by the basis $\{\boldsymbol{e}_r, \boldsymbol{e}_\theta\}$, the strain and stress tensors in this case, removing the out-of-plane component, result in $\boldsymbol{\varepsilon} = [\varepsilon_r, \varepsilon_\theta, 2\varepsilon_{r\theta}]^T$ and $\boldsymbol{\sigma} = [\sigma_r, \sigma_\theta, \sigma_{r\theta}]^T$, while the elasticity tensor $\hat{\boldsymbol{C}}$ defined in equation (1) ($\boldsymbol{S}$ given by equation (2)) is represented in the same basis by the matrix:

$$\hat{\boldsymbol{C}} = \begin{bmatrix} \kappa_r & \sqrt{\kappa_r \kappa_\theta} & 0 \\ \sqrt{\kappa_r \kappa_\theta} & \kappa_\theta & 0 \\ 0 & 0 & 0 \end{bmatrix}. \tag{3}$$

The equation of motion in a solid composed of this particular pentamode material is derived as follows. The constitutive equation and the momentum balance equation for the solid are given by:

$$\boldsymbol{\sigma} = \hat{\boldsymbol{C}} : \boldsymbol{\varepsilon} = \kappa^\star(\boldsymbol{S} : \boldsymbol{\varepsilon})\boldsymbol{S} = -\hat{p}\boldsymbol{S} , \tag{4}$$

$$\rho^\star \cdot \ddot{\boldsymbol{u}} = \mathrm{div}_{\boldsymbol{X}}\boldsymbol{\sigma} = -\boldsymbol{S} \cdot \nabla_{\boldsymbol{X}}\hat{p} , \tag{5}$$

where $\boldsymbol{u}$, $\boldsymbol{\varepsilon}$ and $\boldsymbol{\sigma}$ are the displacements, strain and stress fields, respectively, and

$$\hat{p} = -\kappa^\star(\boldsymbol{S} : \boldsymbol{\varepsilon}) \tag{6}$$

is a pseudo-pressure scalar term. In (4), the trace of the tensorial product between the two second order tensors is denoted by the symbol $(:)$, while the symbol $(\cdot)$

---

[1] In the following, we preserve the name of pentamode material for plane (two-dimensional) problems. Removing the third dimension and the out-of-plane field components, the elasticity tensor has only three eigenvalues. Particularizing the same concept of pentamode material, two of these eigenvalues are related to compliant modes of deformation and only one is related to a hard mode. Strictly, this material should be called bi-mode material.

[2] In this work, the gradient and divergence operators are denoted by $\nabla_{\boldsymbol{X}}(\cdot)$ and $\mathrm{div}_{\boldsymbol{X}}(\cdot)$, respectively. Subindex $\boldsymbol{X}$ emphasizes the coordinate system where they are evaluated.

[3] Voigt or tensorial notation are used indistinctly in this paper. The proper context of every equation determines which specific notation is used.
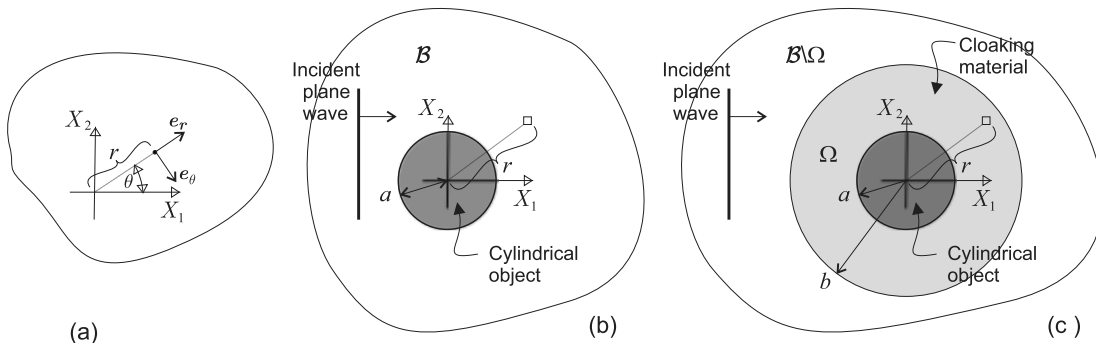
Figure 1: Acoustic cloaking problem. (a) Polar coordinate system; (b) domain of analysis $\mathcal{B}$ with a cylindrical object immersed in the fluid; and (c) cylindrical object with a cloaking device.

indicates the contraction of one index of the tensorial product. In accordance with (4), only stresses proportional to $\boldsymbol{S}$, with the proportionality factor given by pseudo-pressures, can be held by this material. The momentum balance equation (5) is written assuming that the inertial mass density, $\boldsymbol{\rho}^{\star}$, is a generalized second order tensor, not necessarily a spherical one.

After replacing the conventional kinematical compatibility condition $\boldsymbol{\varepsilon} = \frac{1}{2}(\nabla_{\boldsymbol{X}}(\boldsymbol{u}) + \nabla_{\boldsymbol{X}}^{T}(\boldsymbol{u}))$ in equation (4), deriving in time and replacing (5) into (4), a wave propagation equation in terms of the pseudo-pressure field $\hat{p}$ can be derived as follows:

$$\ddot{\hat{p}} - \kappa^{\star}\,\boldsymbol{S} : \nabla_{\boldsymbol{X}}\left((\boldsymbol{\rho}^{\star})^{-1} \cdot \boldsymbol{S} \cdot \nabla_{\boldsymbol{X}}\hat{p}\right) = 0 \ . \tag{7}$$

2.1 Pentamode material for acoustic cloaking devices

Next, let us consider a cylindrical object of radius $r = a$ immersed in a fluid occupying the infinite domain $\mathcal{B}$. The object is reached by an incident plane wave propagating from left to right, as sketched in Figure 1-b. The fluid is characterized by a bulk modulus κ_0 and density ρ_0. We address the problem of designing the pentamode material placed in the circular ring Ω, with exterior radius $r = b$ and thickness $b - a$, acting as the acoustic cloaking device for the cylindrical object, see Figure 1-c.

Equation (7) is utilized in the transformation acoustic analysis by Norris and co-authors (Norris [4] and Gokhale et al. [20]) to define the properties $\kappa^{\star}$, $\boldsymbol{\rho}^{\star}$ and $\boldsymbol{S}$ of a pentamode material which is used to built an acoustic cloaking device adapted for a cylindrical object. Appendix A briefly summarizes Norris's analysis by which the pentamode material parameters for solving this problem are determined. The principal equations being necessary for the following development of the paper are also summarized in Appendix A and have been taken from Gokhale et al. [20].

Considering the large set of possible maps defining a useful coordinate transformation for this problem, Gokhale et al. [20] have defined one transformation preserv-

6

ing the isotropy of the inertial mass density, while keeping the elastic anisotropic properties to a bare minimum (see Appendix A.1). According to these authors, by adopting this particular transformation map and then copying the elastic coefficients of the pentamode material to the geometrical parameters induced by the transformation, the bulk moduli and the inertial mass density of this material result in:

$$\kappa^\star = \kappa_0 \frac{1}{f'(r)}\left(\frac{r}{f(r)}\right) \quad , \quad \kappa_r = \kappa_o \frac{1}{f'(r)}\left(\frac{f(r)}{r}\right) \quad , \quad \kappa_\theta = \kappa_o f'(r)\left(\frac{r}{f(r)}\right) \quad (8)$$

$$\boldsymbol{\rho}^\star = \hat{\rho}\mathbb{1} \quad , \quad \hat{\rho} = \rho_o f'(r)\left(\frac{f(r)}{r}\right) , \quad (9)$$

where r is the radial coordinate as shown in Figure 1-b. The function $f(r)$, defining the coordinate transformation map, is given by:

$$f(r) = \begin{cases} \left(\frac{b^2-a\delta}{b^2-a^2}r - \frac{a-\delta}{b^2-a^2}b^2\frac{a}{r}\right); & a \le r \le b \\ r; & r \ge b \end{cases} \quad (10)$$

with δ being a geometrical parameter whose meaning is discussed in Appendix. Note case that, defining $\mathbb{1}$ as the unit tensor, $\boldsymbol{\rho}^\star$ results in a spherical tensor retrieving the concept of an isotropic inertial mass density. Figure 2-a plots the function $f(r)$ for $\delta = 0.333a$ and $b = 2a$, while Figure 2-b plots the corresponding normalized material properties described in equations (8) and (9) as a function of the radial coordinate.

Then, from expression (3), the elasticity tensor of a pentamode material, whose properties are given by (8) and (9), is defined by:

$$\hat{\boldsymbol{C}} = \kappa_o \begin{bmatrix} \frac{1}{f'(r)}\left(\frac{f(r)}{r}\right) & 1 & 0 \\ 1 & f'(r)\left(\frac{r}{f(r)}\right) & 0 \\ 0 & 0 & 0 \end{bmatrix} . \quad (11)$$

3   Topology optimization problem

The design of the material micro-structure required by Norris's analysis is carried out by defining an appropriate optimization problem which is described in this Section.

Also in this Section, we study the selection of an adequate external shape of the unit cell in where the topology optimization problem is placed. Finally, in sub-Section 3.3, the whole procedure for solving the topology optimization problem is assessed and validated.
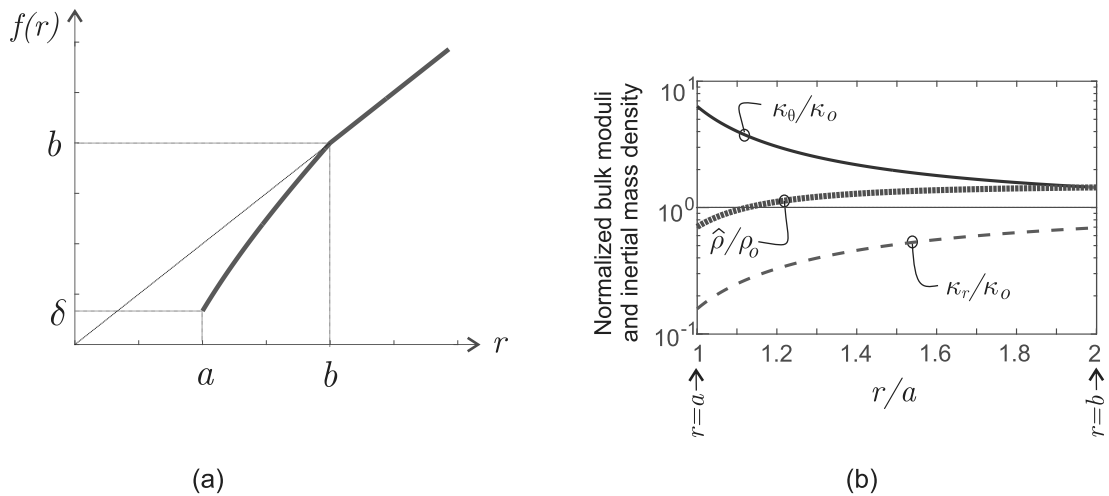
Figure 2: (a) Plot of the function $f(r)$ taken from Gokhale et al. [20]. This function defines the coordinate transformation which is adequate for designing a cylindrical acoustic cloaking layer with minimal elastic anisotropy. (b) Normalized material properties of expressions (8) and (9), derived from the coordinate transformations (27)-(29) (Appendix A) and the parameter $\delta = 0.333a$. The normalization factors are the fluid properties.

3.1 Synthesis of micro-structures as a topology optimization problem

Let us consider a two-phase composite with a periodic micro-structure occupying the macro-scale domain Ω, such as schematized in Figure 3. One phase is assumed to be very stiff and is denoted by M1. The other one is assumed to be very compliant and is denoted by M2. It is assumed that the micro-structure characteristic length, ℓ_{UC}, is much smaller than the characteristic length of the body ℓ [4].
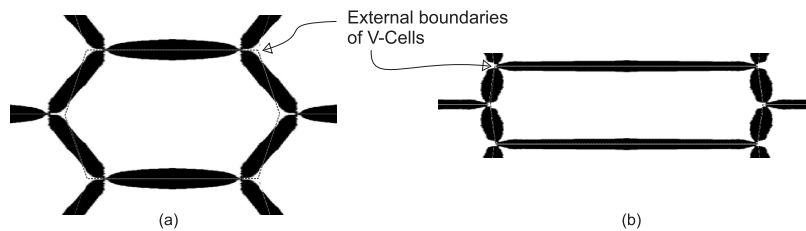

Figure 3: Multiscale material model of a composite with two phases: M1 and M2. Computational homogenization approach to determine $\sigma(\varepsilon)$.

The effective properties of this composite, subjected to elastic loading regimes, are computed via a conventional homogenization technique from a unit-cell denoted

---

[4]In relation to the acoustic cloaking problem here addressed, ℓ can be taken as the cylinder radius.

by Ω_μ. This homogenization technique is briefly explained in Appendix B.1. The effective elasticity tensor $\boldsymbol{C}^{hom}$ obtained through this homogenization technique relates the macro-stress field $\boldsymbol{\sigma}(\boldsymbol{x})$ with the macro-strain field $\boldsymbol{\varepsilon}(\boldsymbol{x})$, as follows:

$$\boldsymbol{\sigma} = \boldsymbol{C}^{hom}(\Omega_\mu^1) : \boldsymbol{\varepsilon} . \tag{12}$$

Denoting Ω_μ^1 and Ω_μ^2 the micro-cell domains occupied by phases M1 and M2, respectively, the argument of $\boldsymbol{C}^{hom}$ remarks its dependence with the material distribution within the unit cell.

Let us now consider a unit-cell, with domain Ω_μ, defined by its external boundary Γ_μ. The material distribution within this domain is determined by solving the following topology optimization problem:

$$\min_{\Omega_\mu^1} \mathcal{J}(\Omega_\mu^1) = \min_{\Omega_\mu^1}(\| \boldsymbol{C}^{hom}(\Omega_\mu^1) - \hat{\boldsymbol{C}} \|^2); \tag{13}$$

where the target tensor $\hat{\boldsymbol{C}}$ is a data of the problem [5], while the conventional Frobenius norm $\| \cdot \|$ computes the distance between $\boldsymbol{C}^{hom}$ and $\hat{\boldsymbol{C}}$. In problem (13), minimization of the objective function $\mathcal{J}(\Omega_\mu^1)$ is attained by changing the placement of material M1 within the domain delimited by Γ_μ.

The optimal distribution of M1 is found with the topology optimization algorithm proposed by Amstutz and Andrä [14] and its extended version [15] particularly adapted to solve inverse material design problems.

Here, the Amstutz's algorithm has been slightly modified to solve the specific problem (13). Some details of this algorithm are presented in Appendix B, while a more fundamental description of the original version can be found in the mentioned bibliography.

The algorithm is implemented with linear triangular finite elements. Therefore, linear polynomials are used to interpolate the level set functions as well as the topological derivative in Ω_μ.

3.2 Selecting an appropriate shape of the boundary Γ_μ

The mathematical problem associated with the topology optimization algorithm is defined in a two-dimensional domain delimited by an external boundary Γ_μ which has to be known in advance. The selection of an adequate shape of Γ_μ is a particularly important issue whenever composites with periodic micro-structures and showing specific symmetries have to be designed.

In this sub-Section, a guideline for solving this issue is given. The idea is inspired by concepts taken from crystallography, Bravais lattices and elastic properties of crystals and also exploits the symmetry shown by the pentamode material.

---

[5]As it is shown in sub-Section 4.2, the target tensor $\hat{\boldsymbol{C}}$ in the acoustic cloaking design problem is given by equation (11)

9

In 2D problems, it has been demonstrated that there are only four different symmetry classes for describing any arbitrary elasticity tensors (see Auffray and Ropars [22] and the references cited therein, as well as Ting [23]). The elasticity tensor $\hat{C}$ of a plane pentamode material, defined in equation (1), has orthotropic (orthorhombic) symmetry denoted by D_2 in Auffray et al. This kind of symmetry is also a characteristic of the elasticity tensors associated with crystalline structures ([24]) that have an atomic distribution placed on the vertices of a (centered rectangular) Bravais lattice having orthogonal primitive vectors $\boldsymbol{a}_1$ and $\boldsymbol{a}_2$, such as shown in Figure 4-a. The lattice parameter $\eta = \|\boldsymbol{a}_1\|/\|\boldsymbol{a}_2\|$ governs approximately the ratio between the coefficients C_{11} and C_{22} of the crystal effective elasticity tensor.

We conjecture that the external boundary Γ_μ coincides with the boundary of a unit-cell utilized in crystallography. In the present case, the unit-cell is taken from a Bravais lattice having orthorhombic symmetry. Figure 4-b shows the Wigner-Seitz unit-cell denoted V-Cell (by Voronoi cell) of a Bravais lattice having this kind of symmetry. It is a non-regular hexagon containing one lattice point (point 0 in Figure 4-a) in the center. The hexagon is built around this point and its sides are the perpendicular bisectors of the segments joining the central point 0 and every one of the other six closest points in the lattice (A, B, C, D, E and F in Figure 4-a).

According to this conjecture, we use V-Cells to represent the boundaries Γ_μ of generic unit-cells associated with pentamode materials. The V-Cell external boundary can be described with only one parameter, such as the lattice parameter η. In Figure 5 are shown several Wigner-Seitz unit-cells for different lattice parameters η, denoted from now on as the shape parameter. For $\eta = \sqrt{3}$, the unit-cell is a regular hexagon, while for $\eta = 1$, it is a square.

From the previous consideration, an isotropic pentamode material should be represented by a regular hexagon defined for the shape parameter $\eta = \sqrt{3}$.

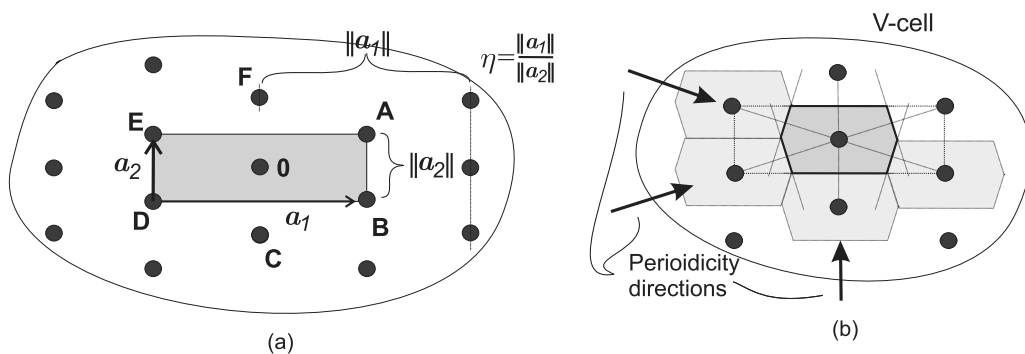
Figure 4: a) Crystal system with orthorhombic symmetry D_2. The associated centered rectangular Bravais lattice has the primitive orthogonal vectors $\boldsymbol{a}_1$ and $\boldsymbol{a}_2$; b) Wigner-Seitz cells (V-Cells) inspiring the selection of the external boundary shape Γ_μ of the unit-cell used for designing the pentamode material. The vectors indicating the periodicity directions are depicted.

Figure 5: Wigner-Seitz cell (V-Cell) for different shape parameters η.

3.3 Validation of the design methodology based on topology optimization

The algorithm presented in Appendix B is validated and assessed through analytical and numerical solutions taken from Sigmund [25]. The proposed problem for this assessment consists in designing the micro-structure topology of an extremal isotropic two-phase material displaying the maximum ratio $\hat{\kappa}/\hat{G}$, where $\hat{\kappa}$ and $\hat{G}$ are the effective bulk and shear moduli of the composite. Sigmund has solved this problem and obtained several micro-structures using a topology optimization tool based on SIMP.

Before presenting the results, a-priori analytical estimations of the bounds for the effective elastic properties of an isotropic composite are discussed. The analyzed composite is constituted by two-phases and bounds, for this kind of composites, have been determined by Hill and successively improved by by Hashin-Shtrikman, Walpole [26] and Cherkaev and Gibiansky [27]. According to the notation utilized by Cherkaev et al., the effective elasticity tensor of a plane strain elastic isotropic material (using Voigt notation for tensors) can be written as:

$$\hat{\boldsymbol{C}}^e = \begin{bmatrix} \hat{K} + \hat{G} & \hat{K} - \hat{G} & 0 \\ \hat{K} - \hat{G} & \hat{K} + \hat{G} & 0 \\ 0 & 0 & \hat{G} \end{bmatrix} \quad , \qquad \hat{K} = \hat{\kappa} + \hat{G}/3 \, , \tag{14}$$

where, as indicated above, $\hat{\kappa}$ and $\hat{G}$ are the effective bulk and shear moduli of the material, and $\hat{K}$ is the plane strain effective bulk modulus. The Hashin-Strikman bounds for a plane elastic isotropic composite with two phases, identified in the following with the numbers 1 and 2, having volume fractions f_1, f_2 and being characterized by the bulk moduli κ_1 and κ_2 and shear moduli G_1 and G_2, respectively, satisfying $\kappa_1 > \kappa_2$ and $G_1 > G_2$, are:

$$K_{HS}^{low} = K_2 + \frac{f_1}{\frac{1}{K_1 - K_2} + \frac{f_2}{K_2 + G_2}} \quad ; \quad K_{HS}^{upp} = K_1 + \frac{f_2}{\frac{1}{K_2 - K_1} + \frac{f_1}{K_1 + G_1}} \quad ; \tag{15}$$

$$G_{HS}^{low} = G_2 + \frac{f_1}{\frac{1}{G_1 - G_2} + \frac{f_2(K_2 + 2G_2)}{2G_2(K_2 + G_2)}} \quad ; \quad G_{HS}^{upp} = G_1 + \frac{f_2}{\frac{1}{G_2 - G_1} + \frac{f_1(K_1 + 2G_1)}{2G_1(K_1 + G_1)}}. \tag{16}$$

Then, the effective plane strain bulk and shear moduli, $\hat{K}$ and $\hat{C}$, of the composite satisfies:

$$K_{HS}^{low} \leq \hat{K} \leq K_{HS}^{upp} \qquad ; \qquad G_{HS}^{low} \leq \hat{G} \leq G_{HS}^{upp}. \qquad (17)$$

Next, let us consider the case studied by Sigmund consisting in finding the micro-structure that provides the maximum possible ratio $\hat{\kappa}/\hat{G}$, agreeing with the analytical estimations of these bounds. In the analysis of Sigmund, here reproduced, both phases are characterized by $K_1 = 5/7$; $K_2 = K_1/20$; $G_1 = 5/13$; $G_2 = G_1/20$ (units of moduli are given in GPa), with the volume fraction $f_1 = 0.5$. Then, the bounds (15)–(16) result in $K_{HS}^{low} = 0.0830$, $K_{HS}^{upp} = 0.2235$, $G_{HS}^{low} = 0.0439$, $G_{HS}^{upp} = 0.1157$. These bounds are represented in Figure 6-a coinciding with the green external box. In the same Figure, the curve corresponding to the improved lower limit bound, found by Cherkaev and Gibiansky [27] has been plotted. The Walpole point is denoted by W_p and has also been plotted in the same Figure. In accordance with these improved bounds, the W_p point determines the maximum ratio $\hat{\kappa}/\hat{G}$ that can be attained with this type of two-phase composite. For the considered composite, the coordinates of the W_p point are $\hat{K}_{W_p} = \hat{K}_{HS}^{upp} = 0.2235$ and

$$G_{W_p} = G_2 + \frac{f_1}{\frac{1}{G_1-G_2} + \frac{f_2(K_1+2G_2)}{2G_2(K_1+G_2)}} = 0.0503 \; . \qquad (18)$$

Therefore, from (14), the effective elasticity tensor of the two-phase composite associated to the W_p point is:

$$\boldsymbol{C}_{W_p} = \begin{bmatrix} 0.2738 & 0.1732 & 0 \\ 0.1732 & 0.2738 & 0 \\ 0 & 0 & 0.0503 \end{bmatrix} . \qquad (19)$$

Procedure for designing the extremal material

The problem (13), constrained by the condition $f_1 = 0.5$, determines the optimal micro-structure topology whose homogenized elasticity tensor, $\boldsymbol{C}^{hom}$, matches the target elasticity tensor: $\hat{\boldsymbol{C}} = \boldsymbol{C}_{W_p}$ of expression (19). This topology optimization problem is solved with the algorithm described in Boxes 1 and 2 of Appendix B. The constraint fixing the volume fraction is imposed to the problem (48) through an augmented lagrangian technique reported in [28] and [29].

Because the target elasticity tensor is isotropic (symmetry $O(2)$ according to [22]), the original domain where the topology optimization algorithm is computed, is the regular hexagon shown in Figure 7. Note that the Wigner-Seitz unit-cell of a Bravais lattice with symmetry $O(2)$ is also a regular hexagon. Additionally, symmetry of the material distribution within the hexagonal unit-cell is imposed by forcing a reflection symmetry of the level-set function respect to the symmetry axis
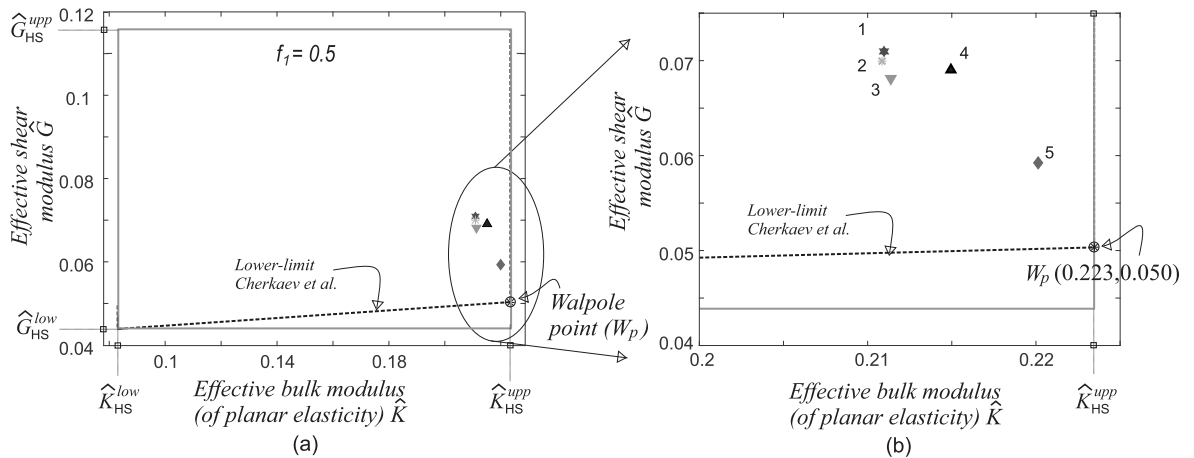
Figure 6: Bounds of effective properties for a two-phase isotropic composite according to Hashin-Shtrikman and Cherkaev et al. Properties of phases 1 and 2 are $K_1 = 5/7$; $K_2 = K_1/20$; $G_1 = 5/13$; $G_2 = G_1/20$ (units of moduli in GPa). Volume fraction of phase 1 is $f_1 = 0.5$. The Walpole point is denoted by W_p. Symbols indicate the effective properties of five microstructures obtained with the topology optimization algorithm.

1-1, 2-2 and 3-3 shown in Figure 7-a. The symmetry is forced in every iteration of the algorithm, after computing (49) in Loop A of Box 2 and before the normalization of ψ^{i+1}.

Results and discussion

Figure (7) shows the micro-structures 1 to 5 that have been obtained with this methodology, using different initializations procedures.

Let us consider the obtained homogenized elasticity tensor corresponding to structure 5:

$$\boldsymbol{C}_5^{hom} = \begin{bmatrix} 0.279 & 0.161 & 0.000 \\ 0.161 & 0.279 & 0.000 \\ 0.000 & 0.000 & 0.059 \end{bmatrix}. \tag{20}$$

The effective parameters $\tilde{G} = C_{33}$ and $\tilde{K} = C_{11} - \tilde{G}$, computed from (20), are plotted in Figure 6. The present approach gives a relative difference of 17% between $\boldsymbol{C}_{W_p}(3,3)$ and $\boldsymbol{C}_5^{hom}(3,3)$. The micro-structures 5 is notoriously similar to that obtained by Sigmund utilizing the SIMP technique.
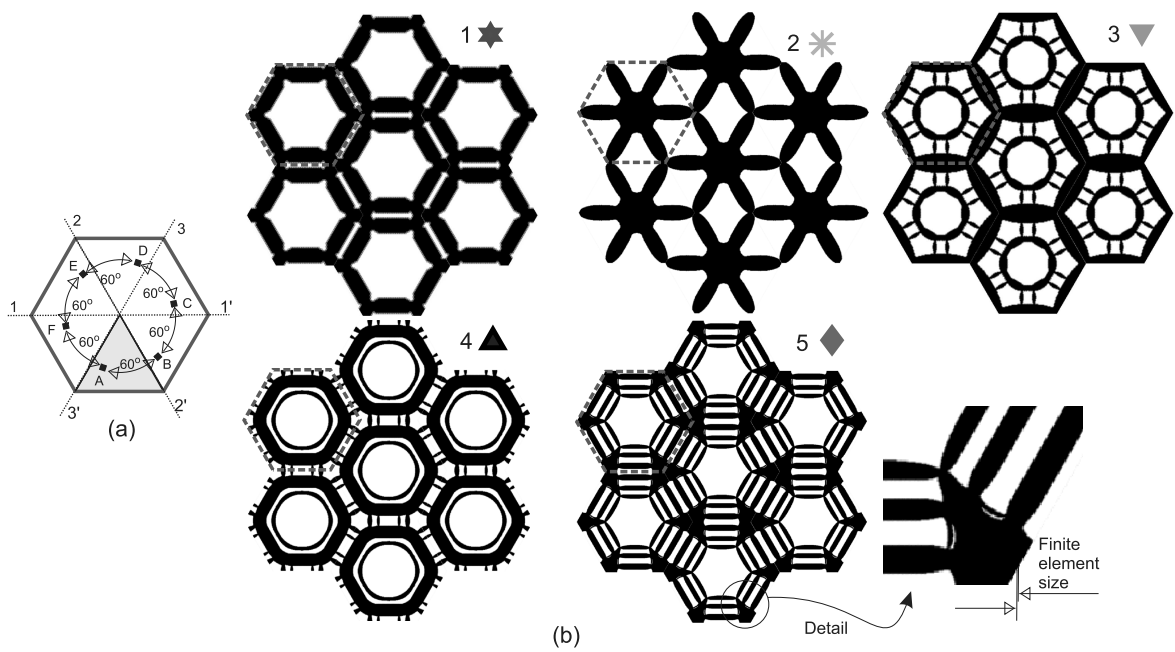
13

Figure 7: a) The material distribution within a unit-cell has reflection symmetry with the symmetry axes being 1-1', 2-2' and 3-3'. b) Micro-structures obtained with the algorithm of Boxes 1 and 2 (Appendix B.3). Elements with negative values of the level set function are in black and show the position where phase M1 is placed.

14

4 Design of the pentamode material for acoustic cloaking

By adopting the analytical results of Gokhale et al. [20], shown in Appendix A.1, we design the micro-structure of a highly anisotropic pentamode metamaterial used as a layer for diminishing the acoustic wave scattering caused by a cylinder immersed in fluids.

4.1 Problem description

A sketch of the addressed problem is shown in Figure 8. The layer covering the cylinder of radius $r = a$ has a thickness which is identical to the cylinder radius ($b = 2a$). The mapping $f(r)$, defining the coordinate transformation in Norris's analysis, is given by equation (10) (see also Appendix A) with the parameter $\delta = 0.333a$. With this parameter, the effective scattering cross section area of the cloaked object has to be similar to that produced by a bare cylinder of radius $a_r = \delta = 0.333a$.
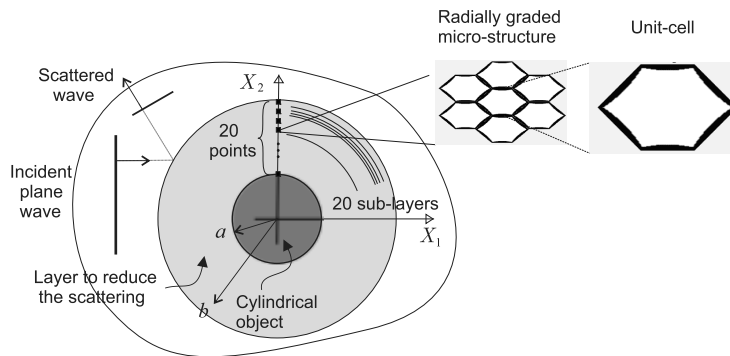

Figure 8: Scattering reduction layer.

We design 20 unit-cells of the graded layer in correspondence with the same quantity of radial points equally spaced between $r = a$ and $r = b = 2a$. We assume that the graded layer is composed of 20 uniform sub-layers which micro-structures are designed with those 20 cells.

The stiff phase of the synthesized material (material M1) is assumed to be aluminum with properties $\kappa_{Al} = 70.GPa$, $G_{Al} = 25.5GPa$ and $\rho_{Al} = 2700.Kg/m^3$. The soft phase (material $M2$) is assumed to be a flexible polymer foam characterized by an isotropic material whose elastic modulus has a contrast factor $\gamma = 0.00001$ times the elastic modulus of the aluminum (taken from Ashby [30], pp.51).

4.2 General design procedure

The procedure guiding the design of the micro-structures of each sub-layer aims to satisfy point-wise the following two conditions:

i) The effective elasticity tensor $\boldsymbol{C}^{hom}$ of the synthesized composite matches the target tensor $\hat{\boldsymbol{C}}$ defined in (11) for the corresponding sub-layer. Note that this tensor is described in the coordinate system whose basis is: $(\boldsymbol{e}_r, \boldsymbol{e}_\theta)$.

ii) The effective inertial mass density ρ^{hom} of the same unit-cell matches the target inertial mass density $\hat{\rho}$ defined by equation (9).

Both goals can be attained in two sequential steps. The first step searches the optimal distribution of phase M1 satisfying the objective described in task *i)* without imposing the density constraint. This problem is formulated as a topology optimization problem and solved with the algorithm of Appendix B.3. The solution provides a homogenized density ρ^{OT} which is assumed to satisfy $\rho^{OT} < \hat{\rho}$. This is a reasonable assumption which can be satisfied by taking an enough high ratio E_1/ρ_1 of the material M1 (aluminum in this case).

In a second step, the micro-cell density is adjusted to $\hat{\rho}$. This objective is attained by filling the holes (soft phase) with a composite constituted by the phase M1 dispersed in the phase M2. In this case, the disperse dense material does not work as a structural component and the effective elasticity is not substantially modified. We assume that the second step can be easily solved. Therefore, in the following, we only address the topology optimization problem associated with the first step.

A similar design procedure in two sequential steps has been reported by Kadic et al. [9]. To build a pentamode material, these authors have independently adjusted the effective bulk moduli in a first stage, and then, the effective inertial mass density. Additionally, they have proven the fabricability of the so-designed metamaterial by manufacturing small samples.

4.3 Technique for adjusting the anisotropic bulk moduli

The external boundary Γ_μ delimiting the domain Ω_μ, in where the topology optimization problem is posed, has to be known in advance. Due to the symmetry of the target tensor $\hat{\boldsymbol{C}}$ (orthotropic symmetry D_2), V-Cells with given shape parameters η are chosen. In each case, η is adjusted for each sub-layer of the 20 designed cells.

Influence of the shape parameter η on the resulting micro-structures

To better understand the role played by the selection of Γ_μ and the shape parameter η in the present design technique, we study the influence of this parameter on the obtained micro-structure solution.

Sub-layer number 15 of the acoustic cloaking device is chosen to perform this study. For this sub-layer, the target elasticity tensor $\hat{\boldsymbol{C}}$ is given by the expression (see equation (11)):

$$\hat{\boldsymbol{C}} = \begin{bmatrix} 5.893 & 2.250 & 0 \\ 2.250 & 0.859 & 0 \\ 0 & 0 & 0 \end{bmatrix}. \tag{21}$$

V-Cell geometries, as shown in Figure 4, are tested. Then, the optimal solutions of problem (13) are sought by varying the parameter η in the range: $1 \leq \eta \leq 8$.

In Figure 9-a, the optimal value of $\mathcal{J}$ attained for different parameters η are plotted. Two finite element meshes are solved. Results obtained with the coarse mesh (with $m_{max} = 3$ and $h_0^e = \ell_{UC}/32$) are denoted by (CM), while those obtained with the finest one, $m_{max} = 4$, are denoted by (FM). We recall that m_{max} defines the number of mesh refinements and h_0^e is the initial finite element mesh size. Both parameters have been defined in Box 1 (Appendix B.3). The finite element size of the finest mesh is half of that of the coarse mesh.

In the same Figure, the effective elasticity tensor component C_{33}^{hom} and the homogenized inertial mass density ρ^{OT} of the designed cell (Figures 9-b and c, respectively) are also plotted. We recall that the effective densities plotted in Figures 9-c, are the results of the topology optimization problem (13) without imposing a density constraint.
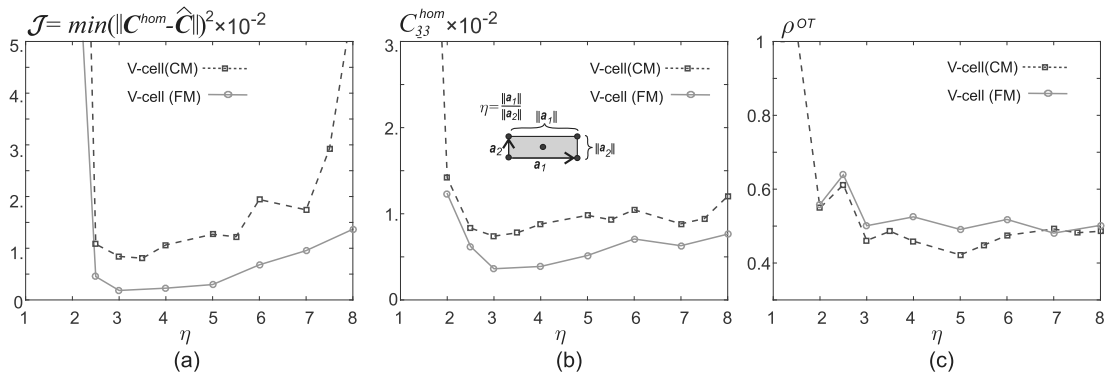

Figure 9: Two set of solutions attained with finite element mesh refinement, CM and FM denote coarse and fine mesh, respectively. V-Cells are characterized with the shape parameter η: a) optimal attained value of $\mathcal{J}$ defined in problem (13); b) Shear stiffness C_{33} of the effective attained elasticity tensor; c) effective attained inertial mass density ρ^{OT}.

Results in Figure 9 show a rather sensitive response with respect to changes of the shape parameter η. The minimal shear modulus C_{33}^{hom} and the minimal objective function value $\mathcal{J}$ are attained in the range $3 \leq \eta \leq 5$. Also, note that in the same range of η, the effective inertial mass density is almost constant around $\rho^{OT} = 0.5$.

It is noted that the correct capturing of the effective shear modulus of the sub-layer, represented by the term C_{33}^{hom}, is crucial to get a good response of the cloaking device. According to Norris's analysis, this term has to be zero.

Figure 10 displays the micro-structures and the corresponding effective elasticity tensors obtained as solution of the topology optimization problem computed with four V-Cell geometries. In all cases, except in the result with $\eta = 2$, we have obtained good agreement between $\boldsymbol{C}^{hom}$ and the target tensor defined in expression (21).
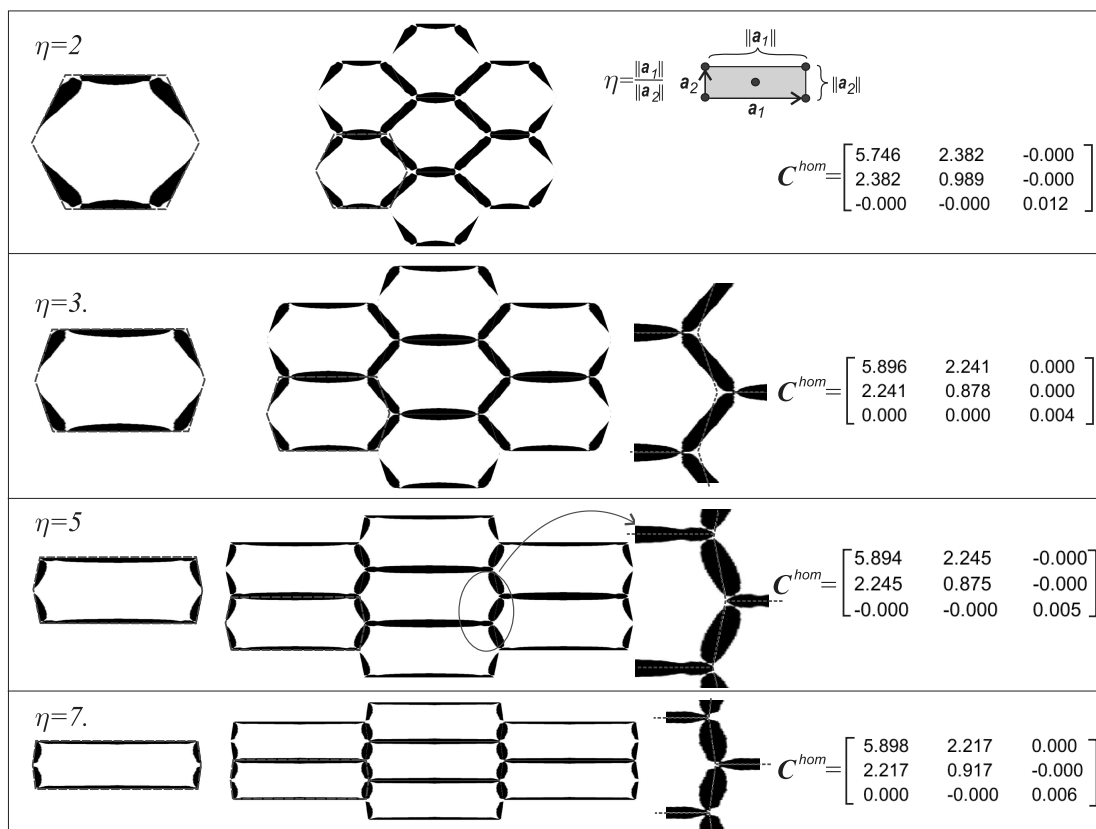
Figure 10: Microstructures for sub-layer number 15 obtained with V-Cells (FM) and varying the shape parameter η. The first column displays the unit-cells and the solutions provided by the topology optimization algorithm. The second column displays the resulting micro-structures obtained by the spatial repetition of the computed unit-cell. The third column (cases with $\eta = 3, 5$ and 7) displays details of the joints between needle-like members. The last column shows the computed effective elasticity tensors.

Conclusions of the study about the influence of η on the microstructure design are summarized as follows:

- As the finite element mesh is refined (m_{max} is increased), better solutions to

18

problem (13) are obtained. However, the crucial conclusion is that the shape of Γ_μ is of paramount importance to obtain good solutions. Tests conducted with rectangular unit-cell shapes, using different slenderness ratios, yield unsatisfactory results.

- From Figure 9, the range of parameters $3 \leq \eta \leq 5$ provides good approaches to the solution of the topology optimization problem. Notably, however, geometries defined with $\eta < 2.5$, that correspond to squares or regular hexagons, are excluded from the admissible configurations and must be avoided.

- There are several micro-structure architectures providing effective elasticity tensors $\boldsymbol{C}^{hom}$ approaching the target one. It is the case of the microstructures depicted in Figure 11. Then, it can be concluded that the problem (13) has not a unique solution and that several material architectures are admissible for the present acoustic cloaking device.

- In most cases observed in Figures 10, the external boundaries of the V-Cells do not coincide well with the hexagonal cells displayed by the obtained honeycomb-like micro-structures. For example, for the microstructures depicted in Figure 11, we have detected that for $\eta \approx \hat{C}_{11}/\hat{C}_{22} \approx 7$ (Figure 11-b), the V-Cell captures almost exactly the geometry of the basic cell. However, this configuration does not lead to the better solution. The best solution is obtained for $\eta \approx 3.75$ (Figure 11-a).
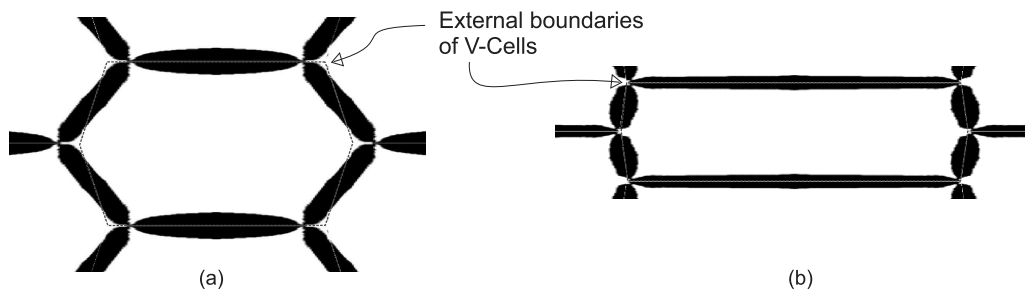

Figure 11: Two possible micro-structures for sub-layer 15 obtained with V-Cells characterized with the shape parameters: a) $\eta = 3$ and b) $\eta = 7$.

4.4 Results of the designed acoustic cloaking device

From the exposed conclusions in the previous sub-Section and in order to avoid a similar study for the 20 sub-layer designs, we solve these topology optimization

problems by adopting V-Cell geometries whose shape parameters are defined through a relation depending on the coefficients of the target elasticity tensor, as follows:

$$\eta = \sqrt{3}\left(1 + 0.2\frac{\hat{C}_{11} - \hat{C}_{22}}{\hat{C}_{22}}\right).$$

This criterion is taken by considering the following empirical rules: for an isotropic pentamode material, with $\hat{C}_{11}/\hat{C}_{22} = 1$, the V-Cell should be a regular hexagon defined by $\eta = \sqrt{3}$. While for $\hat{C}_{11}/\hat{C}_{22} \approx 6.9$, that corresponds to the sub-layer 15 studied in the previous sub-Section, the V-Cell should be defined by $\eta = 3.75$, which has proven to give the most optimal solution.

Figure 12 shows the micro-structures of sub-layers 1, 5, 10, 15 and 20, obtained with this procedure. The second column displays details of the synthesized micro-structures such as the needle-like members and joints. The third column shows the effective elasticity tensors $\boldsymbol{C}^{hom}$ and densities ρ^{OT} compared with the target elasticity tensors $\hat{\boldsymbol{C}}$ and target densities $\hat{\rho}$ for these sub-layers.

As commented above, the solutions for the 20 cells provide homogenized mass densities which are lower than the ones required by Norris's analysis. Therefore, in the validation test of next Section, we assume that these densities could be exactly adjusted to the target values.

Figure 13 plots the effective properties κ_r^{hom}, κ_θ^{hom} and C_{33}^{hom} for the synthesized 20 sub-layers.

5   Scattering performance assessment of the designed layer

The performance of the metamaterial designed with the technology of the previous Section, whose properties are plotted in Figure 13, is next assessed in the following examples.

This performance is evaluated by studying the scattering wave field produced by a plane wave impinging on a cloaked cylindrical object immersed in an infinite fluid medium. The cloaking device being designed with a parameter $\delta = 0.333m$ has to affect the external wave field, outside the cloak region, as much as a bare cylindrical object of radius $a_r = 0.333m$. Then, the goal of the present validation test consists in comparing the scattered wave field for both cases.

Considering the excessively high computational cost required by a detailed DNS simulation (Direct Numerical Simulation) of this problem including the modeling of the material micro-structure and its interaction with the fluid, we simulate a simplified verification test. The acoustic cloaking device is modeled with 20, layers perfectly connected, made of elastic materials whose properties are identical to the effective ones determined with the design methodology of the previous Section.
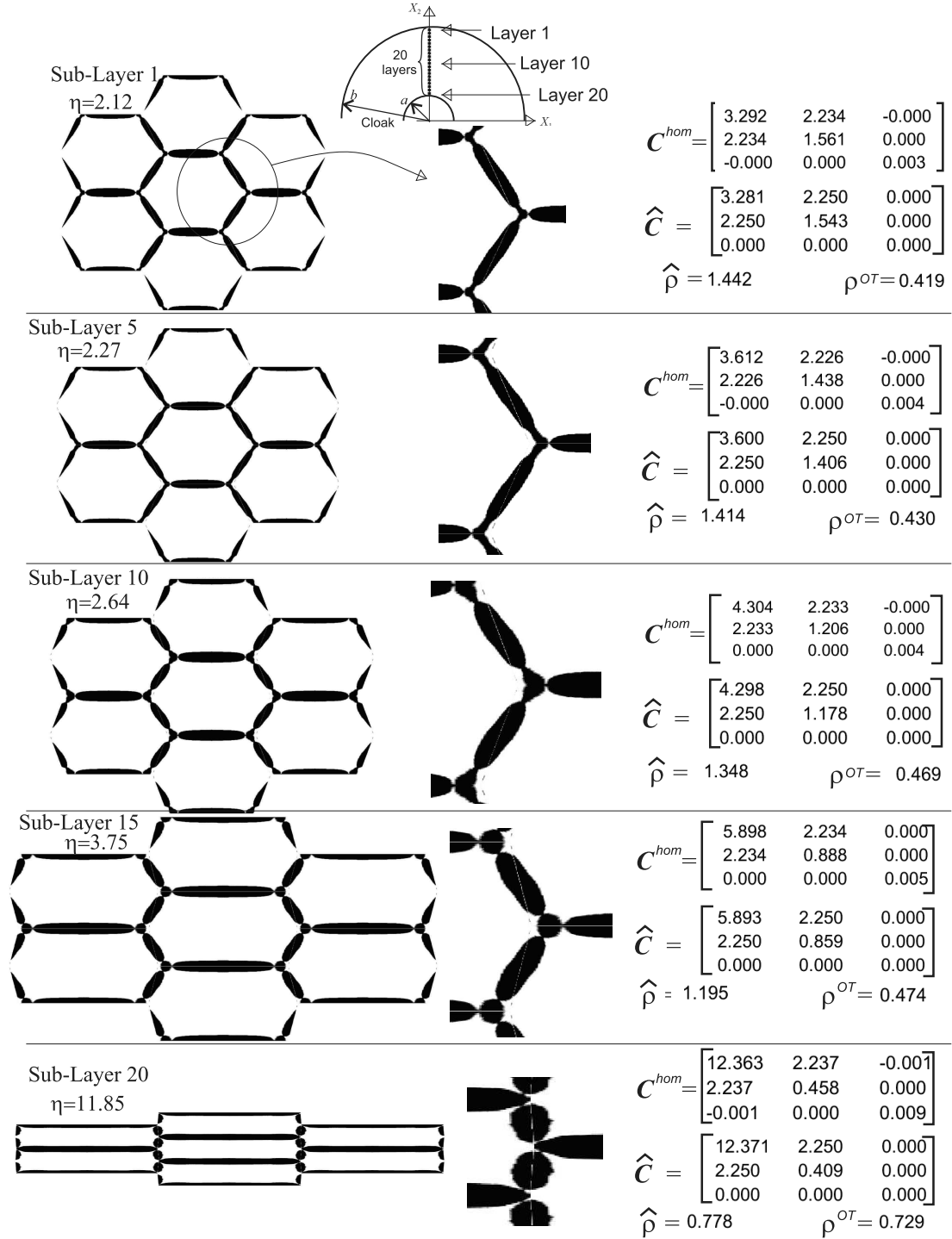
Sub-Layer 1
$\eta=2.12$

20 layers

Cloak

X_2

Layer 1
Layer 10
Layer 20

X_1

$$C^{hom}=\begin{bmatrix} 3.292 & 2.234 & -0.000 \\ 2.234 & 1.561 & 0.000 \\ -0.000 & 0.000 & 0.003 \end{bmatrix}$$

$$\widehat{C}=\begin{bmatrix} 3.281 & 2.250 & 0.000 \\ 2.250 & 1.543 & 0.000 \\ 0.000 & 0.000 & 0.000 \end{bmatrix}$$

$$\widehat{\rho}=1.442 \qquad \rho^{OT}=0.419$$

Sub-Layer 5
$\eta=2.27$

$$C^{hom}=\begin{bmatrix} 3.612 & 2.226 & -0.000 \\ 2.226 & 1.438 & 0.000 \\ -0.000 & 0.000 & 0.004 \end{bmatrix}$$

$$\widehat{C}=\begin{bmatrix} 3.600 & 2.250 & 0.000 \\ 2.250 & 1.406 & 0.000 \\ 0.000 & 0.000 & 0.000 \end{bmatrix}$$

$$\widehat{\rho}=1.414 \qquad \rho^{OT}=0.430$$

Sub-Layer 10
$\eta=2.64$

$$C^{hom}=\begin{bmatrix} 4.304 & 2.233 & -0.000 \\ 2.233 & 1.206 & 0.000 \\ 0.000 & 0.000 & 0.004 \end{bmatrix}$$

$$\widehat{C}=\begin{bmatrix} 4.298 & 2.250 & 0.000 \\ 2.250 & 1.178 & 0.000 \\ 0.000 & 0.000 & 0.000 \end{bmatrix}$$

$$\widehat{\rho}=1.348 \qquad \rho^{OT}=0.469$$

Sub-Layer 15
$\eta=3.75$

$$C^{hom}=\begin{bmatrix} 5.898 & 2.234 & 0.000 \\ 2.234 & 0.888 & 0.000 \\ 0.000 & 0.000 & 0.005 \end{bmatrix}$$

$$\widehat{C}=\begin{bmatrix} 5.893 & 2.250 & 0.000 \\ 2.250 & 0.859 & 0.000 \\ 0.000 & 0.000 & 0.000 \end{bmatrix}$$

$$\widehat{\rho}=1.195 \qquad \rho^{OT}=0.474$$

Sub-Layer 20
$\eta=11.85$

$$C^{hom}=\begin{bmatrix} 12.363 & 2.237 & -0.001 \\ 2.237 & 0.458 & 0.000 \\ -0.001 & 0.000 & 0.009 \end{bmatrix}$$

$$\widehat{C}=\begin{bmatrix} 12.371 & 2.250 & 0.000 \\ 2.250 & 0.409 & 0.000 \\ 0.000 & 0.000 & 0.000 \end{bmatrix}$$

$$\widehat{\rho}=0.778 \qquad \rho^{OT}=0.729$$

Figure 12: Solutions obtained with the topology optimization algorithm for several sub-layers of the acoustic cloaking device. C^{hom} and ρ^{OT} are the effective elasticity tensors and homogenized densities of the micro-cells obtained with the topology optimization algorithm. $\widehat{C}$ and $\widehat{\rho}$ are the target effective elasticity tensors and densities according to Norris's analysis.
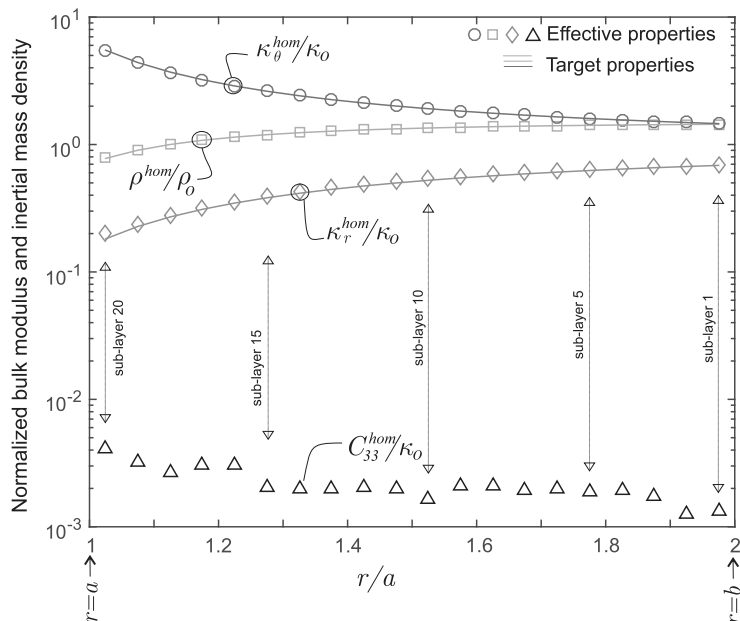
21

Figure 13: Normalized effective properties of the 20 sub-layers obtained with the topology optimization algorithm. The bulk moduli κ_r^{hom} and κ_θ^{hom}, the inertial mass densities ρ^{hom} and shear moduli C_{33}^{hom} are shown in symbols. Curves in line are the analytical expression taken from Figure 2.

Figure 14 displays the pressure maps (real part) for several cases of the mentioned problem computed with an in-house finite element code. This code solves the wave equation problem in the frequency domain and utilizes a Perfectly Matched Layer (PML) technique for modeling the infinite domain of the fluid. Pressure maps in the Figure are the results of an incident plane wave, from the left. The wave frequency is $2.07Khz$ (angular frequency: $\omega = 1.3e4 rad/s$) and the medium, across which the wave propagates, is water with a density $\rho_0 = 1000.Kg/m^3$ and a volumetric modulus $\kappa_0 = 2.25GPa$. The wave speed in this medium is $c_0 = 1500.m/seg$ and the wave number for this frequency is $k = \omega/c_0 = 8.67 rad/m$ with a wavelentgth $\lambda = 2\pi/k = 0.72m$. The analyzed domain has a size of $10.m \times 10.m$.

Solutions are computed and compared for different cases:

i) object with perfect cloak designed according to analytical results of Norris;

ii) bare object of radius $a = 1.m$;

iii) object of radius $a = 1.m$ with the cloaking device designed in accordance with the topology optimization technique and the parameter $\delta = 0.333m$;

iv) bare object of radius: $a_r = 0.333m$.

22

We recall that the external domain solution of case *iii)* should mimic the solution of case *iv)*.

In order to quantitatively compare the solutions presented in Figure 14, the effective cross section areas are computed in the last three cases. Let us consider again a plane wave traveling from left to right in a free infinite medium with a vertical wavefront. The pressure response in the time domain $(\boldsymbol{X}, t)$ can be expressed by:

$$p^i(\boldsymbol{x}, t) = p_0 \exp\left(i(\boldsymbol{k} \cdot \boldsymbol{X} - \omega t)\right) \tag{22}$$

where, recalling that k is the wave number, $\boldsymbol{k} = k\boldsymbol{e}_x$ is the wave vector, and $\boldsymbol{e}_x$ is the unit vector in the horizontal direction. The rigid cylindrical object of radius $a = 1.m$ is placed at $\boldsymbol{X} = \boldsymbol{0}$. The cloak occupies the space $\Omega = \{\boldsymbol{X} \mid 1.m \leq \|\boldsymbol{X}\| \leq 2.m\}$. The object produces a scattered wave field which, at large distances from the cylinder, can be assumed as spherical wave field centered at $\boldsymbol{X} = \boldsymbol{0}$. The pressure field, $p(\boldsymbol{X}, t)$, resulting from the incident and scattered waves is computed in the frequency domain with the finite element code. By considering that $p_w(\boldsymbol{X})$ denotes the amplitude of the pressure field in the frequency domain, the effective cross section area (per unit of thickness) of the object is evaluated as follows:

$$\sigma^{eff} = \int_{\mathcal{S}} \frac{(\Delta p_w)(\overline{\Delta p_w})}{p_w^i \overline{p_w^i}} d\mathcal{S} \quad ; \quad \Delta p_w(\boldsymbol{X}) = p_w(\boldsymbol{X}) - p_w^i(\boldsymbol{X}) \tag{23}$$

where the integration curve $\mathcal{S}$ is a circle of radius $r = 4.5m$ and the symbol $(\bar{\cdot})$, over both terms in the integrand, represents the complex conjugate of the magnitude.

Figure 15-a depicts, in a polar plot, the integrand value of expression (23) along the curve $\mathcal{S}$ as a function of the angular position θ. Three curves corresponding to cases *ii)*, *iii)* and *iv)* are shown. Figure 15-b depicts a zoom of the polar plot in where only the case *iii)* and *iv)* are shown. Note that the cloaked cylinder of radius $a = 1$ generates a scattered wave field, with notably lower values of the integrand term if compared with the bare cylinder of the identical radius. Furthermore, the integrand value distribution is qualitatively identical to that produced by a significantly smaller object.

Figure 15-c plots the effective cross-section areas (per unit of thickness of the object) for the three cases: *ii)*, *iii)* and *iv)* and different frequencies of the incident plane wave. These results quantify the capability of the designed cloak at different wave frequencies. They confirm that, in a wide range of frequencies, the cloaking device is almost insensitive to this variable.

5.1   Modal analysis of a micro-cell

Considering that the micro-structure of the designed material consists of slender bars with a filler polymer possessing a very low stiffness and a dense disperse phase,
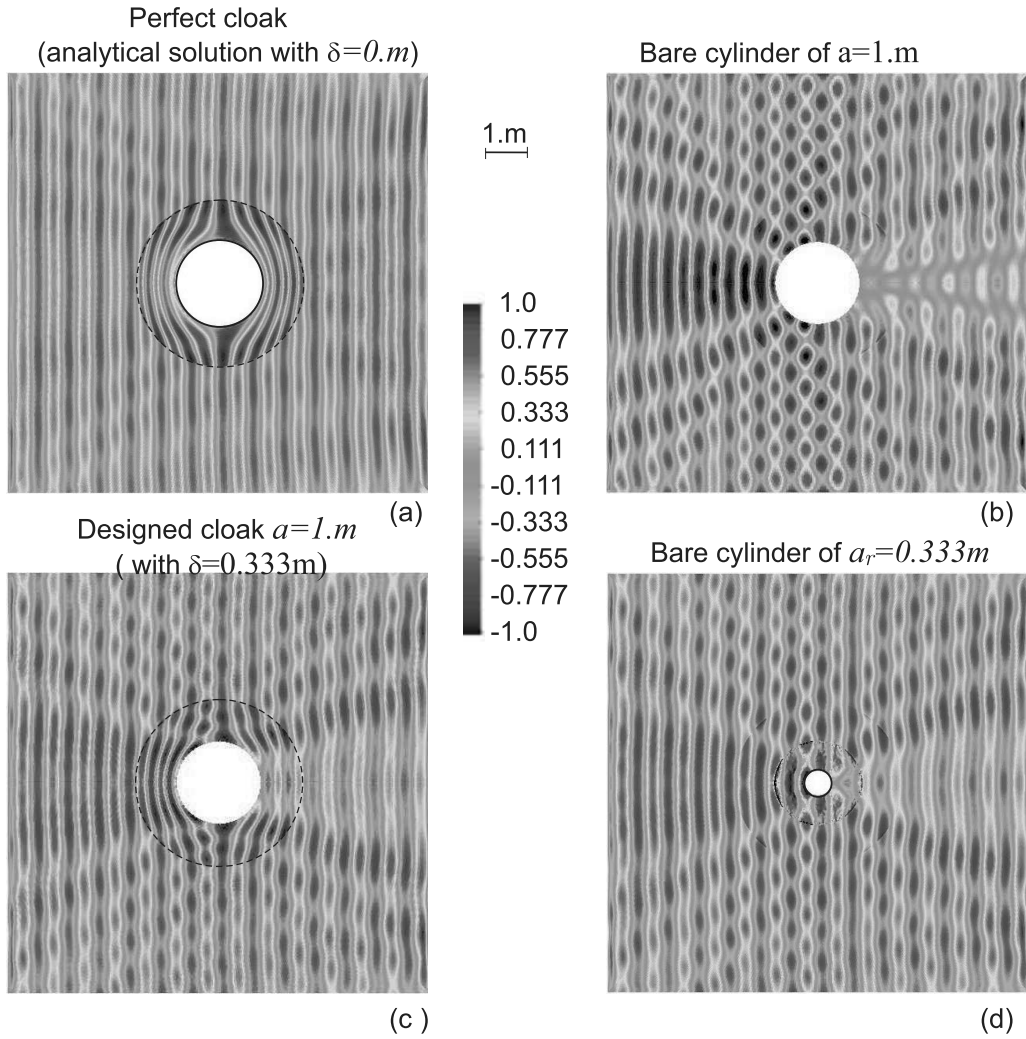
Figure 14: Pressure maps (real part) of an incident plane wave problem. Domain size: $10.m \times 10.m$, wave angular frequency: $\omega = 1.3e4rad/s$. a) Solution of the cylinder with radius $a = 1m$ and perfect cloaking (parameter $\delta = 0.m$). The material properties of the cloak are given by Norris's analysis in Appendix A.1; b) solution with a bare cylinder of radius $a = 1.m$; c) cylinder of radius $a = 1m$ with the designed acoustic cloaking using the parameter $\delta = 0.333m$; d) solution with a bare cylinder of radius $a_r = 0.333m$.
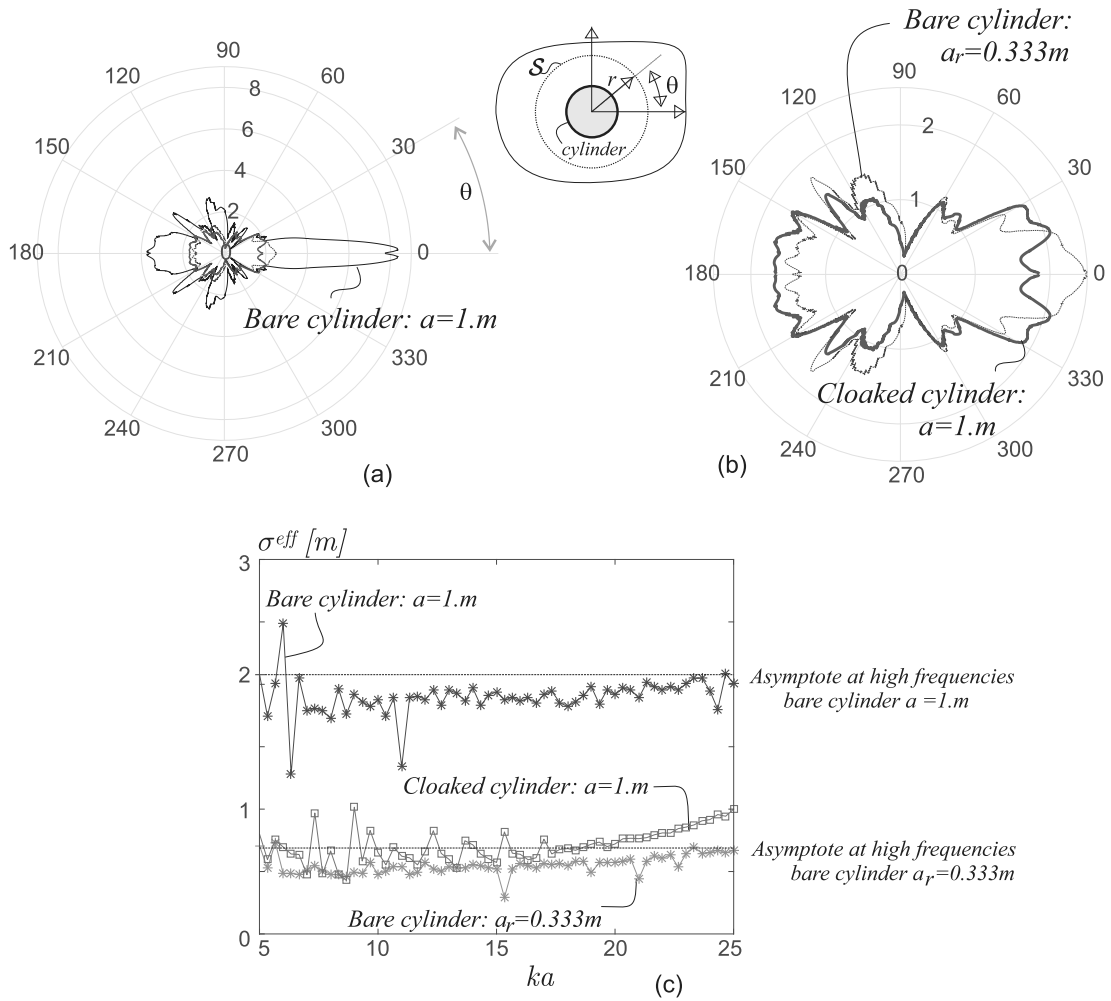
Figure 15:   a) Polar plots of the integrand in (23) corresponding to the cases: *ii), iii)* and *iv)*; b) zoom of the polar plot shown in (a) displaying the cases *iii)* and *iv)*; c) Effective cross-section areas (per unit of thickness) for cases *ii), iii)* and *iv)* computed for different wave numbers of the incident wave.

it is necessary to guarantee that the lower eigenfrequencies of the unit-cell are much higher than the frequency of the sound wave. This requirement should be satisfied to guarantee that the static homogenization analysis, implicitly considered in this paper, is a valid assumption of the model and that the natural frequencies of the cloak do not interfere the sound wave.

The unit-cell eigenfrequencies increase with the inverse of the cell size. Therefore, it can be guaranteed that the above requirement is satisfied for small enough cell sizes. The maximum cell size of the designed pentamode material is limited by the acoustic wavelength and by the thickness of the layers in which the cloaking device is divided. The shortest wavelength in the analysis of Figure 15 is $0.25m$ and the layer thickness, by assuming an identical value for all layers, is $0.05m$.

In view of the above discussion, the modal analysis of the unit-cell of layer 1 is subsequently performed. In the context of evaluating minimal eigenfrequencies of the designed micro-structures, this layer is the most compromised one. Figures 16-a and b show the finite element model of the analyzed cell and the adopted geometrical dimensions. A characteristic cell size of $0.01m$ is arbitrarily chosen. Two cases are solved. In the first one, the polymer, as well as the dynamical effect of the disperse phase are neglected. In the second case, all the components are considered.

In accordance with the cell designed for layer 1, in Figure 16, the density provided by the solution of the topology optimization algorithm is $\rho^{OT} = 389.kg/m^3$. The target density is $\hat{\rho} = 1442.kg/m^3$. Therefore, by taking a polymer density $\rho_{Pol} = 20.Kg/m^3$ and the aluminum density $\rho_{Al} = 2700.kg/m^3$, the target density $\hat{\rho}$ is get by dispersing a volume fraction $f_{Al} = 0.2642$ of aluminum into the polymer. The disperse aluminum phase is modeled by assigning the aluminum properties to finite elements randomly placed into the space which is originally occupied by the polymer, until the required volume fraction is reached. Therefore, due to the fact that the cell volume is $1.06e - 4m^2$ and the number of finite elements is 11911, the mean size of the aluminum particles used in the analysis is $8.9e - 09m^2$.

Periodic boundary conditions are imposed to the finite element model of the unit cell Note that the acoustic wavelengths are much larger than the cell size.

The obtained results in both cases are: a) the lower eigenfrequency when the polymer and disperse phase is neglected is $79kHz$. b) the lower eigenfrequency when the polymer and disperse phase is taken into account is $75kHz$. Then, both frequencies result much higher than the sound wave frequencies considered in the analysis of the previous sub-Section.

The eigenmode related to the lower eigenfrequency for the case a) is depicted in Figure 16-c.

These results confirms that, for cell sizes smaller than $0.01m$, the homogenization static analysis followed in this paper is a valid assumption.
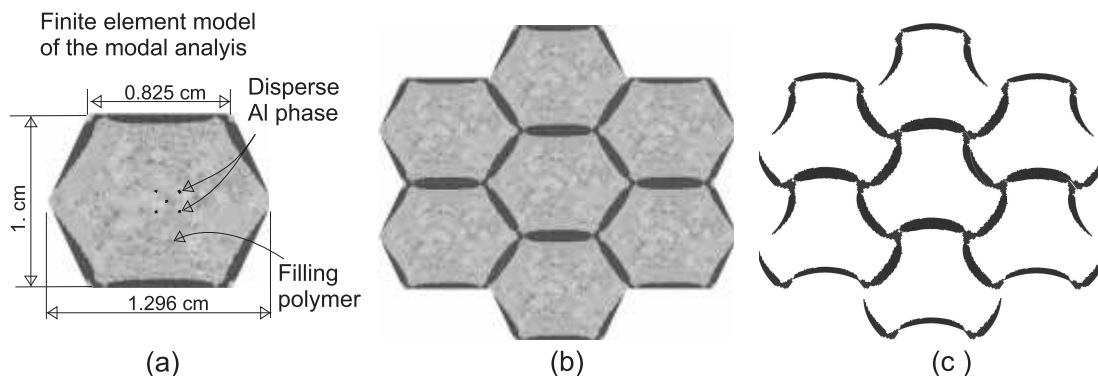
Figure 16: Modal analysis of the unit cell taken from layer 1 of the cloaking device. a-b) Finite element model. c) Eigenmode corresponding to the lower eigenfrequency when polymer and disperse phase effects are neglected.

6   Conclusions

The results presented in this work show the viability of using topology optimization techniques based on topological derivative to design the micro-structures of a graded layer for acoustic cloaking devices. The manufacturing feasibility of such layers, employing available materials, has been already proven.

To attain such results, it has been imperative to properly select a unit-cell geometry where the topology optimization problem is posed. In this sense, it has been shown that the material symmetry can be properly exploited to solve this issue. The presented study has provided additional ingredients to understand the influence of the unit-cell external shape on the results obtained with the optimization algorithm. From this study, it has been proven that solutions strongly depend on this variable, and that square or regular hexagonal shapes have to be discarded in several cases.

The validation test proves the effectiveness of the synthesized composite for satisfying the target proposed for the cloaking device. This virtual test shows a significant decrease of the scattered wave power produced by the immersed cloaked object. The pattern of the scattered wave agrees acceptably well with the ideal case of an immersed bare object with reduced dimensions.

An additional conclusion refers to the wide range of metamaterial design problems in which this type of framework can be applied. The most promising application field is related to metamaterial design problems whose micro-structure architecture cannot be conjectured beforehand. Typical cases are the design of: *i)* extreme materials with large negative Poisson ratios, *ii)* ultralight and ultra stiff metamaterials, *iii)* material for thermal flux manipulation, between others. Progress in the synthesis of ultralight and ultra stiff structures using this type of computational design tool has been presented by the authors in [31].

27

Finally, a potential improvement of this technology can be identified by introducing the notion of topological derivatives of anisotropic elastic materials. Some of the authors of this paper have recently published a work with contributions in this topic, see Giusti et al. [29]. This derivative, within the context of topology optimization, opens the possibility to design metamaterials through several length scales.

Acknowledgments

A   APPENDIX: Linear acoustic theory and field transformation analysis

Let us consider a conventional acoustic wave problem propagating in a fluid medium at rest and placed in an homogeneous domain $\tilde{\mathcal{B}}$, see Figure 1. In this medium, κ_0 denotes the time-averaged bulk modulus and ρ_0 denotes the time-averaged density. The disturbance produced by the wave motion superposed to the time-averaged fields are assumed small. Then, the linear acoustic wave equation in terms of the pressure field $P(\tilde{\boldsymbol{X}}, t)$ can be written as ([32]):

$$\ddot{P} - \kappa_0 \operatorname{div}_{\tilde{\boldsymbol{X}}}(\rho_0^{-1}\nabla_{\tilde{\boldsymbol{X}}}P) = 0 \ . \tag{24}$$

In the present description, $\tilde{\mathcal{B}}$ refers to the homogeneous space because the wave propagate with null scattering strength. $\tilde{\mathcal{B}}$ is also assumed as the reference space for the transformation to be defined in the following.

Following to Norris [4], the form-invariance property of equation (24) is next exploited. Let us consider the physical space $\mathcal{B}$, where some object is immersed in the fluid, and the coordinate system $\boldsymbol{X}$ in $\mathcal{B}$. The physical space is mapped from the reference space through a coordinate transformation, $\boldsymbol{X} = \phi(\tilde{\boldsymbol{X}})$, sketched in Figure 17. The map ϕ is assumed to be one-to-one and invertible, except at possibly one point in the domain $\Omega \subset \tilde{\mathcal{B}}$. The deformation gradient of ϕ ($\phi : \tilde{\mathcal{B}} \to \mathcal{B}$) is: $\boldsymbol{F} = \nabla_{\tilde{\boldsymbol{X}}}\phi.$

Then, equation (24) can be re-written in the physical frame $\boldsymbol{X}$ by introducing the tensorial transformations of the differential operators: $\text{div}_{\boldsymbol{X}}(\cdot)$ and $\nabla_{\boldsymbol{X}}(\cdot)$, in terms of $\text{div}_{\tilde{\boldsymbol{X}}}(\cdot)$ and $\nabla_{\tilde{\boldsymbol{X}}}(\cdot)$. These tensorial transformations can be derived by introducing the deformation analysis, within the context of finite elasticity, described in the book of Ogden [33]. The resulting wave propagation equation in the physical domain is given as follows:

$$\ddot{p} - \kappa_0 J \,\text{div}_{\boldsymbol{X}}\left((\rho_0 J)^{-1} \boldsymbol{V}^2 \cdot \nabla_{\boldsymbol{X}} p \right) = 0 \tag{25}$$

where $\boldsymbol{V}^2 = \boldsymbol{F}\boldsymbol{F}^T$, $J = \det(\boldsymbol{F})$ and the pressure in the physical space is denoted by $p(\boldsymbol{X}, t)$.

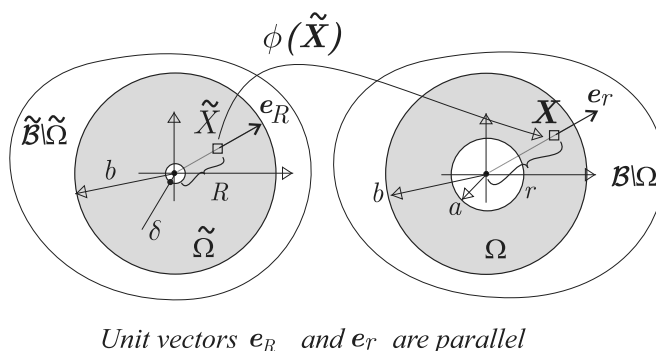Unit vectors $\boldsymbol{e}_R$ and $\boldsymbol{e}_r$ are parallel

Figure 17: Radially symmetric deformation map. Homogeneous ($\tilde{\mathcal{B}}$) and physical ($\mathcal{B}$) spaces.

However, and following to Norris, a more general and adequate expression of the acoustic wave equation (24) in the physical space can be defined by introducing a second order symmetric tensor field $\boldsymbol{\Sigma}$, such that: $\text{div}_{\boldsymbol{X}}\boldsymbol{\Sigma} = \boldsymbol{0}$. In this case, equation (25) can be equivalently rewritten as:

$$\ddot{p} - \kappa_0 J \boldsymbol{\Sigma} : \nabla_{\boldsymbol{X}}\left((\rho_0 J \boldsymbol{\Sigma})^{-1} \cdot \boldsymbol{V}^2 \cdot \nabla_{\boldsymbol{X}} p \right) = 0 \tag{26}$$

At every point of $\mathcal{B}$, it can be recognized the similar form displaying the pseudo-pressure wave equation (7), which represents an acoustic wave propagating across a pentamode material, and the acoustic wave equation (26) in the transformed space. Both equations can be made identical under the condition that the parameter of the geometrical transformations, given by the map $\boldsymbol{\phi}$ in (26), are reinterpreted as being the heterogeneous properties of the pentamode material defined in Section 2. This condition is satisfied if the following constraints on the material properties are imposed point-wise:

i) $\boldsymbol{S} \equiv \boldsymbol{\Sigma}$,

ii) $\kappa^\star = \kappa_0 J$, and

iii) $\boldsymbol{\rho}^\star = \rho_0 J \boldsymbol{\Sigma} \cdot \boldsymbol{V}^{-2} \cdot \boldsymbol{\Sigma}$.

29

With this redefinition of the pentamode material properties in $\boldsymbol{X}$, the wave equation in $\mathcal{B}\backslash\Omega$ mimics the wave equation in the reference empty space $\tilde{\mathcal{B}}\backslash\tilde{\Omega}$.

A.1 A radially symmetric deformation map for cylindrical object cloaking

Let us consider an acoustic wave propagating in a medium where a cylindrical object of radius a is immersed, as shown in Figure 1-b. Our goal is to design the properties of the metamaterial filling the circular ring domain Ω, of thickness $b - a$, around the cylinder such that it acts as a cloaking for the object. In this way, the wave propagating at the exterior domain $\mathcal{B}\backslash\Omega$ is not affected by the object.

This goal can be reached by exploiting the results of the previous sub-Section. Let a radially symmetric deformation map be given by:

$$\boldsymbol{X} = \phi(\tilde{\boldsymbol{X}}) = \frac{r(R)}{R}\tilde{\boldsymbol{X}} \tag{27}$$

where R and r are the radial coordinates of two points: $\tilde{\boldsymbol{X}}$ and $\boldsymbol{X}$ ($R = \left\|\tilde{\boldsymbol{X}}\right\|$ and $r = \|\boldsymbol{X}\|$) in the reference and physical spaces, respectively, related through the map (27). The radial unit vectors in both spaces are defined by:

$$\frac{\boldsymbol{X}}{r} = \boldsymbol{e}_r = \boldsymbol{e}_R = \frac{\tilde{\boldsymbol{X}}}{R} \; ; \tag{28}$$

The radial coordinate $r(R)$ is defined by the inverse function:

$$R = f(r) = \begin{cases} \left(\frac{b^2 - a\delta}{b^2 - a^2}r - \frac{a - \delta}{b^2 - a^2}b^2\frac{a}{r}\right); & a \leq r \leq b \\ r; & r \geq b \end{cases} \tag{29}$$

The interpretation of this deformation map is sketched in Figure 17. This function transforms the circular ring domain $\tilde{\Omega}$, of thickness $b - \delta$, in another circular ring Ω, of thickness $b - a$, while the exterior domain $\mathcal{B}\backslash\Omega$ is identically mapped.

By considering a null parameter δ for this transformation, the map (27)-(29) is singular at the origin and the cylinder acoustic cloaking, associated with this transformation, is perfect. To avoid the singularity, we assume a value: $\delta > 0$. In this case, the effective cross-section of the immersed object is reduced if compared with that of the bare cylinder. Therefore, the device built with the so-idealized pentamode material work as a scattering reduction layer instead of as a perfect cloaking device.

The function (29) is taken from Gokhale et al. [20] and, according to these authors, satisfies the criteria by which the cloaking material properties show minimal elastic anisotropy.

30

Further identities involving the gradient of deformation of $\boldsymbol{\phi}$ and the associated right stretch tensor are derived from (28) and (29) as follows:

$$\boldsymbol{F} = \frac{1}{f'(r)}\boldsymbol{I}_r + \frac{r}{f(r)}\boldsymbol{I}_\perp \qquad ; \qquad \boldsymbol{I}_r = \boldsymbol{e}_r \otimes \boldsymbol{e}_r \qquad ; \qquad \boldsymbol{I}_\perp = \mathbb{1} - \boldsymbol{e}_r \otimes \boldsymbol{e}_r; \tag{30}$$

$$J = \det(\boldsymbol{F}) = \frac{1}{f'(r)}\left(\frac{r}{f(r)}\right)^{(n_d-1)} \tag{31}$$

where we consider a two-dimensional space, with $n_d = 2$.

Furthermore, we choose:

$$\kappa^\star = \kappa_0 J = \kappa_0 \frac{1}{f'(r)}\frac{r}{f(r)}\,, \tag{32}$$

and:

$$\boldsymbol{S} = \left(\frac{f(r)}{r}\right)\left(\boldsymbol{I}_r + \frac{rf'(r)}{f(r)}\boldsymbol{I}_\perp\right). \tag{33}$$

Note that the divergence-free condition of the field $\boldsymbol{S}$ follows from equation (33).

From expressions (32), (33) and (1), the moduli of the elastic constitutive tensor κ_r and κ_θ in equation (3), result in:

$$\kappa_r = \kappa_o \frac{1}{f'(r)}\left(\frac{f(r)}{r}\right) \qquad ; \qquad \kappa_\theta = \kappa_o f'(r)\left(\frac{r}{f(r)}\right) \tag{34}$$

and therefore:

$$\hat{\boldsymbol{C}} = \begin{bmatrix} \frac{1}{f'(r)}\left(\frac{f(r)}{r}\right) & 1 & 0 \\ 1 & f'(r)\left(\frac{r}{f(r)}\right) & 0 \\ 0 & 0 & 0 \end{bmatrix}. \tag{35}$$

Also, the inertial mass density is given by:

$$\boldsymbol{\rho}^\star = \rho_o f'(r)\left(\frac{f(r)}{r}\right)\mathbb{1} \tag{36}$$

In this case, $\boldsymbol{\rho}^\star$ results in a spherical tensor, and therefore:

$$\rho_r = \rho_\theta = \rho = \rho_o f'(r)\frac{f(r)}{r}\,. \tag{37}$$

With these definition of the material parameters at the cloak, and the condition: $f(r = b) = b$, the radial impedance and the circumferential wave speed at the interface separating both domains, medium and cloak, are identical:

$$Z_r^{\text{cloack}}(r = b) = \sqrt{\kappa_r \rho} = \sqrt{\kappa_o \rho_o} = Z_r^{\text{medium}}(r = b); \tag{38}$$

$$c_\theta^{\text{cloack}}(r = b) = \sqrt{\kappa_\theta/\rho} = \sqrt{\kappa_o/\rho_o} = c_\theta^{\text{medium}}(r = b)\,. \tag{39}$$

B Topology optimization algorithm for inverse design of the micro-structure

In this Appendix, the most salient points of topology optimization algorithm utilized for micro-structure inverse design are discussed. These points include the computational homogenization technique (sub-Section B.1), which is used to evaluate the effective properties of the composite, the topological derivative of the homogenized elasticity tensor described in sub-Section B.2, and the optimization algorithm summarized in two Boxes 1 and 2 of sub-Section B.3. Also, the modification of some key aspects of the topology optimization algorithm are included in order to adapt this algorithm to the acoustic cloaking design problem.

B.1 Computational homogenization

Let us consider the two-phase composite schematized in Figure 3 with a periodic micro-structure represented through a unit cell denoted by Ω_μ.

The macro-strain and macro-stress fields described at Ω are denoted by $\boldsymbol{\varepsilon}$ and $\boldsymbol{\sigma}$, respectively. The same fields observed at the micro-scale Ω_μ are denoted by $\boldsymbol{\varepsilon}_\mu$ and $\boldsymbol{\sigma}_\mu$. These terms are represented in Figure 3-a, where the homogenization procedure is also sketched.

A linear elastic response for every phase of the composite at the micro-scale is assumed. It is expressed by:

$$\boldsymbol{\sigma}_\mu(\boldsymbol{y}) = \boldsymbol{C}_\mu(\boldsymbol{y}) : \boldsymbol{\varepsilon}_\mu(\boldsymbol{y}) , \tag{40}$$

where $\boldsymbol{C}_\mu(\boldsymbol{y})$ is the elasticity tensor of the corresponding phase at point $\boldsymbol{y}$. Then, a macroscopic linear constitutive relation, $\boldsymbol{\sigma} = \boldsymbol{C}^{hom} : \boldsymbol{\varepsilon}$, is inherited, whose effective elasticity tensor is denoted by $\boldsymbol{C}^{hom}$. The tensor $\boldsymbol{C}^{hom}$ is evaluated by following conventional computational homogenization techniques imposing periodic boundary conditions at Γ_μ, see [34]. Due to the assumed linearity of the relation $\boldsymbol{\sigma}(\boldsymbol{\varepsilon})$, we compute the homogenized constitutive tensor evaluating three homogenized macro-stresses, $\boldsymbol{\sigma}_1$, $\boldsymbol{\sigma}_2$ and $\boldsymbol{\sigma}_3$ for specific macro-strains $\boldsymbol{\varepsilon}_1$, $\boldsymbol{\varepsilon}_2$ and $\boldsymbol{\varepsilon}_3$. The three strains $\{\boldsymbol{\varepsilon}_1, \boldsymbol{\varepsilon}_2, \boldsymbol{\varepsilon}_3\}$, given by: $\boldsymbol{\varepsilon}_1 = \boldsymbol{e}_r \otimes \boldsymbol{e}_r$, $\boldsymbol{\varepsilon}_2 = \boldsymbol{e}_\theta \otimes \boldsymbol{e}_\theta$ and $\boldsymbol{\varepsilon}_3 = 1/2(\boldsymbol{e}_r \otimes \boldsymbol{e}_\theta + \boldsymbol{e}_\theta \otimes \boldsymbol{e}_r)$, define a canonical basis of the macro-strain space. In Voigt notation, the j-th basis of these strain tensors can be written as: $\boldsymbol{\varepsilon}_j = [(\varepsilon_j)_{rr}, (\varepsilon_j)_{\theta\theta}, 2(\varepsilon_j)_{r\theta}]^T$.

Then, the matrix of the elasticity tensor is given by:

$$\boldsymbol{C}^{hom} = [\boldsymbol{\sigma}_1(\boldsymbol{\varepsilon}_1), \boldsymbol{\sigma}_2(\boldsymbol{\varepsilon}_2), \boldsymbol{\sigma}_3(\boldsymbol{\varepsilon}_3)] . \tag{41}$$

So, the j-th column of $\boldsymbol{C}^{hom}$ is the macro-stress $\boldsymbol{\sigma}_j(\boldsymbol{\varepsilon}_j)$ computed as the volumetric average of the micro-stress $(\boldsymbol{\sigma}_\mu)_j$:

$$\boldsymbol{\sigma}_j(\boldsymbol{\varepsilon}_j) = \frac{1}{|\Omega_\mu|} \int_{\Omega_\mu} (\boldsymbol{\sigma}_\mu)_j \, d\Omega_\mu . \tag{42}$$

The micro-stress $(\boldsymbol{\sigma}_\mu)_j$ results from solving the unit-cell boundary value problem briefly defined as follows:

i) the macro-strain $\boldsymbol{\varepsilon}_j$ is uniformly distributed into the unit-cell domain Ω_μ. This term operates as the driving force of the mechanical problem formulated at the unit-cell;

ii) the micro-strain field, $(\boldsymbol{\varepsilon}_\mu)_j$, in Ω_μ is the addition of two terms: $(\boldsymbol{\varepsilon}_\mu)_j = \boldsymbol{\varepsilon}_j + (\tilde{\boldsymbol{\varepsilon}}_\mu)_j$. The last term, $(\tilde{\boldsymbol{\varepsilon}}_\mu)_j$, is a kinematically compatible micro-strain fluctuation field;

iii) micro-stress $(\boldsymbol{\sigma}_\mu)_j$ is a self-equilibrated stress field satisfying anti-periodic traction boundary conditions and the elastic constitutive relation (40).

Additional details of this homogenization procedure can be obtained in the reference works de Souza Neto and Feijóo [34].

The rule of mixtures is the homogenization technique adopted for evaluating the effective inertial mass density ρ^{hom}.

B.2 Topological derivative of the homogenized elasticity tensor

The unit-cell domain Ω_μ considered in the previous sub-Section is separated in two disjoint domains: Ω_μ^1 and Ω_μ^2, occupied by phase M1 and M2, respectively ($\Omega_\mu = \Omega_\mu^1 \cup \Omega_\mu^2$), see Figure 18.

Phase M1 is an isotropic elastic material whose elastic modulus and Poisson's ratio are denoted by E_μ^1 and ν_μ^1. Phase M2 is also an isotropic elastic material whose elastic modulus and Poisson's ratio are defined by: $E_\mu^2 = \gamma E_\mu^1$ and $\nu_\mu^2 = \nu_\mu^1$, where the parameter γ is the stiffness contrast ratio between phases M1 and M2.
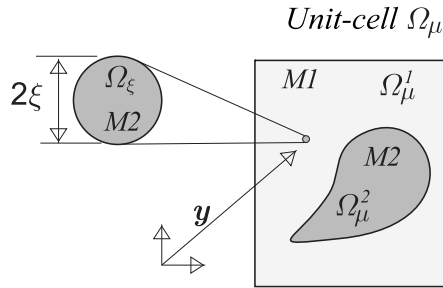

Figure 18: Multiscale material model of a composite with two phases: M1 and M2. The topological derivative $D_T \boldsymbol{C}^{hom}(\boldsymbol{y})$ of the homogenized elasticity tensor $\boldsymbol{C}^{hom}(\boldsymbol{y})$ gives its sensitivity to material distribution changes within the micro-cell.

For a given distribution of phases, let us consider the homogenized constitutive tensor $\boldsymbol{C}^{hom}$. The topological derivative of $\boldsymbol{C}^{hom}$, denoted by $D_T\boldsymbol{C}^{hom}$, at point $\boldsymbol{y}$ occupied by phase M1, is the fourth order tensor representing the sensitivity of $\boldsymbol{C}^{hom}$ to the nucleation of a circular perturbation around $\boldsymbol{y}$. The perturbation consists in substituting a ball of material M1 and radius ξ by an identical ball constituted of material M2. The ball area $|\Omega_\xi|$ is the perturbation parameter. Alternatively, if $\boldsymbol{y}$ refers to a point occupied by phase M2, the topological derivative indicates the sensitivity of nucleating a circular perturbation of material M1.

The mathematical meaning of the topological derivative can be illustrated through the asymptotic expansion of the effective elasticity tensor $\boldsymbol{C}^{hom}_{pert}$ which is the homogenized tensor after introducing the perturbation. This asymptotic expansion is developed in terms of the area $|\Omega_\xi|$ and is written as follows:

$$\boldsymbol{C}^{hom}_{pert} = \boldsymbol{C}^{hom} + \frac{|\Omega_\xi|}{|\Omega_\mu|}D_T\boldsymbol{C}^{hom}(\boldsymbol{y}) + \mathcal{O}\left(\frac{|\Omega_\xi|}{|\Omega_\mu|}\right). \tag{43}$$

The last term in (43) is an infinitesimal of order two in the argument. Further details about the meaning of (43) can be found in [15] and [35].

Using Voigt notation for fourth order tensors, the (i,j)-th component of the topological derivative matrix $(i,j = 1, ..., 3)$, denoted by $[D_T\boldsymbol{C}^{hom}]_{ij}$, is computed through the following expression:

$$[D_T\boldsymbol{C}^{hom}]_{ij} = -\frac{\chi_1}{E_\mu^1}\Big(4(\boldsymbol{\sigma}_\mu)_i : (\boldsymbol{\sigma}_\mu)_j - \chi_2 \text{tr}((\boldsymbol{\sigma}_\mu)_i)\text{tr}((\boldsymbol{\sigma}_\mu)_j)\Big), \tag{44}$$

where

$$\chi_1 = \frac{1-\gamma}{1+\tau\gamma} \ , \ \ \chi_2 = \frac{1-\gamma(\tau-2\zeta)}{1+\zeta\gamma} \ \ , \ \ \tau = \frac{1-\nu_\mu^1}{1+\nu_\mu^1} \ , \ \ \zeta = \frac{3-\nu_\mu^1}{1+\nu_\mu^1} \ ,$$

while $(\boldsymbol{\sigma}_\mu)_i$ and $(\boldsymbol{\sigma}_\mu)_j$ are the micro-stress fields utilized in the integrand of equation (42). These stresses are the solution of the micro-cell problem defined in the previous sub-Section.

Equation (44) has been derived by implicitly assuming that a ball of material M2 is introduced into the domain M1. Alternatively, if the perturbation consist of introducing a small ball of material M1 into the domain M2, the role of E_μ^1, E_μ^2 and γ in equation (44) should be exchanged to compute $D_T\boldsymbol{C}^{hom}$ in that position (E_μ^2 takes the role of E_μ^1 and γ is redefined as: $\gamma = E_\mu^2/E_\mu^1$).

B.3   Topology optimization algorithm based on the Amstutz's procedure

The algorithm for solving the problem (13) relies on two ingredients:

a) A continuous function $\psi(\boldsymbol{y})$ (with $\psi \in L^2(\Omega_\mu)$) which zero level set represents the geometry of the interface M1-M2. It is called the level set function and is defined by:

$$\psi(\boldsymbol{y}) := \left\{ \begin{array}{llll} < 0 & ; & \forall & \boldsymbol{y} \in \Omega_\mu^1 \ ; \\ > 0 & ; & \forall & \boldsymbol{y} \in \Omega_\mu^2 \ . \end{array} \right. \tag{45}$$

where sub-domains Ω_μ^1 and Ω_μ^2 have been previously defined.

b) The topological derivative $g(\boldsymbol{y})$ which is defined as follows:

$$g(\boldsymbol{y}) := \left\{ \begin{array}{llll} -D_T\mathcal{J}(\boldsymbol{y}); & \text{if:} & \boldsymbol{y} \in \Omega_\mu^1 \ ; \\ D_T\mathcal{J}(\boldsymbol{y}); & \text{if:} & \boldsymbol{y} \in \Omega_\mu^2 \ . \end{array} \right. \tag{46}$$

The topological derivative of the objective function (13), considering the Frobenius norm, results in:

$$D_T\mathcal{J}(\boldsymbol{y}) = 2 \left(\boldsymbol{C}^{hom} - \hat{\boldsymbol{C}} \right) : D_T\boldsymbol{C}^{hom}(\boldsymbol{y}) \ , \tag{47}$$

and this functions can be computed after replacing $D_T\boldsymbol{C}^{hom}$ by the term defined in (44).

In the Amstutz's approach, the function ψ of the optimal solution of a topology optimization problem is found through a fixed point iteration and the topological derivative, providing a descent direction of the objective function.

This algorithm has been slightly adapted to dealt with the objective function described in the problem (13). It is described in the following Boxes 1 and 2.

Box 1: Topology Optimization Algorithm defined in Ω_μ:
Given:
 - one initial finite element mesh of size h_0^e,
 - a trial level set function $\psi_0(h_0^e)$, and $m = 0$.
Compute $\boldsymbol{C}^{hom}(\psi_0(h_0^e))$ and the sequence of tensors $\check{\boldsymbol{C}} = \{\check{\boldsymbol{C}}_1, ..., \check{\boldsymbol{C}}_\ell, ...\check{\boldsymbol{C}}_{n_c}\}$
      described by equation (50), and then:

DO LOOP 1 (mesh refinement loop): m-index: from 0 to m_{max}
     DO LOOP 2 (sequence of $\check{\boldsymbol{C}}_\ell$ toward $\hat{\boldsymbol{C}}$): ℓ-index: from 1 to n_c
        Evaluates a new ψ_ℓ by solving:

$$\psi_\ell(h_m^e) = arg\{\min_{\psi_\ell} \mathcal{J}(\psi_\ell)\} = arg\{\min_{\psi_\ell}(\|\boldsymbol{C}^{hom}(\psi_\ell) - \check{\boldsymbol{C}}_\ell\|)^2\}, \qquad (48)$$

        using the algorithm in BOX 2
     END LOOP 2

     Performs a finite element mesh refinement, $h_{m+1}^e \leftarrow h_m^e/2$
     Project $\psi_{n_c}(h_m^e)$ to the new mesh: $\psi_0(h_{m+1}^e) \leftarrow \psi_{n_c}(h_m^e)$
     Compute: $\boldsymbol{C}^{hom}(\psi_0(h_{m+1}^e))$
     Compute a new sequence $\check{\boldsymbol{C}}$ (equation (50))
END LOOP 1

Box 2: Algorithm for solving problem (48)
Given a trial level set function: $\psi^i = \psi_{\ell-1}$

DO LOOP A: (i-index increases):
     Select a step length ξ (line search), then compute:

$$\hat{\psi}^{i+1} = \psi^i + \xi \, \frac{g(\psi^i)}{\alpha}, \text{ and normalize: } \psi^{i+1} = \frac{\hat{\psi}^{i+1}}{\|\hat{\psi}^{i+1}\|_{L^2}} \qquad (49)$$

     Compute: $\mathcal{J}(\psi^{i+1})$ and $g(\psi^{i+1})$

     IF: $\mathcal{J}(\psi^{i+1})$ satisfies the convergence criterion:
           STOP: the algorithm converges and the solution is: $\psi_\ell = \psi^{i+1}$
     ENDIF

END LOOP A

Description of Box 1: the procedure consists of two nested loops:

1) (LOOP 1) The external loop handles a finite element mesh refinement sequence. The parameter m_{max} identifies the maximum number of times that the mesh is refined during the solution process. Then, each finite element mesh, in the refinement sequence, is identified by a characteristic mesh size: h_m^e where sub-index m denotes the m-th loop. The level set function ψ is defined in each node of the finite element mesh. Then, the dependence of the level set function ψ with the finite element mesh is remarked using the notation $\psi(h_m^e)$, where h_m^e represents the finite element mesh size at loop m.

2) The field $\psi(h_m^e)$ is determined by solving the problem (13) with the target elasticity tensor $\hat{\boldsymbol{C}}$. This field is found through a sequence of n_c sub-problems solved in the inner loop (LOOP 2). The level set function solution of every sub-problem (ψ_ℓ) is identified with a sub-index coinciding with the inner loop index. So, $\psi_0(h_m^e)$ represents the trial level set function for the mesh of size h_m^e, while $\psi_{n_c}(h_m^e)$ is the solution obtained after solving n_c sub-problems.

In the inner loop, each sub-problem is similar to (13) but with a redefined target elasticity tensor. For each sub-problem, the target elasticity tensor is taken from a convex combination of $\boldsymbol{C}^{hom}(\psi_0(h_m^e))$ and $\hat{\boldsymbol{C}}$ as follows:

$$\check{\boldsymbol{C}}_\ell = \left(\frac{n_c - \ell}{n_c}\right) \boldsymbol{C}^{hom}(\psi_0(h_m^e)) + \left(\frac{\ell}{n_c}\right) \hat{\boldsymbol{C}} \ . \tag{50}$$

The notation adopted in this equation emphasizes the fact that $\boldsymbol{C}^{hom}$ depends on the level set function determining the topology of the cell Ω_μ.

The tensor $\check{\boldsymbol{C}}_\ell$ is utilized to compute the objective function $\mathcal{J}$, and the corresponding topological derivative, of the ℓ-th sub-problem in the inner loop as follows:

$$\mathcal{J} = (\|\boldsymbol{C}^{hom}(\psi) - \check{\boldsymbol{C}}_\ell\|)^2 \ , \tag{51}$$

which is solved with the algorithm presented in Box 2. Observe that for $\ell = n_c$ is $\check{\boldsymbol{C}}_{n_c} = \hat{\boldsymbol{C}}$. Then, the last internal loop solves the original problem (13).

Description of Box 2: the iterative algorithm for solving the level set function $\psi_\ell(h_m^e)$, of the sub-problem (48), utilizes a fixed point iteration. The topological derivative $g(\psi)$ is used as a feasible descent direction to optimize $\mathcal{J}(\Omega_\mu^1)$ in problem (13) (additional details about this important point can be found in [14] and [15]). The normalization factor α is chosen to avoid the ill-conditioning happening in points close to the solution of problem (48). Note that $\|g\|_{L^2} \to 0$ as: $\boldsymbol{C}^{hom}(\psi) \to \check{\boldsymbol{C}}_\ell$. The value α is selected as the average of $\|g\|_{L^2}$ in the initial iterations of the loop in Box 2.

Step length selection (ξ) and convergence criterion in Box 2

37

The step length ξ is found through a line search defined by:

$$\xi = arg \, (\min_{\tilde{\xi} \in \mathcal{I}_\xi} \mathcal{J}(\psi_{\tilde{\xi}}^{i+1})) \tag{52}$$

with

$$\hat{\psi}_{\tilde{\xi}}^{i+1} = \psi^i + \tilde{\xi} \, \frac{g(\psi^i)}{\alpha} \qquad , \qquad \psi_{\tilde{\xi}}^{i+1} = \frac{\hat{\psi}_{\tilde{\xi}}^{i+1}}{\|\hat{\psi}_{\tilde{\xi}}^{i+1}\|_{L^2}}$$

and the parameters $\tilde{\xi}$ are taken from the set of numbers defined by:

$$\mathcal{I}_\xi := [\xi_{min} : \Delta\xi : \xi_{max}] \quad ; \quad \Delta\xi = \frac{\xi_{max} - \xi_{min}}{10}$$

where ξ_{min} and ξ_{max} are the minimum and maximum allowed step lengths which are taken as $\xi_{min} \ll 1$ and $\xi_{max} = 1$, respectively, and $\Delta\xi$ is a predefined increment of the step length.

The stop criterion is given by:

$$|\mathcal{J}(\psi^{i+1}) - \mathcal{J}_{10}| < tol \tag{53}$$

where $\mathcal{J}_{10}$ is the average of $\mathcal{J}$ in the last 10 iterations and *tol* is an absolute tolerance.

The initialization of the algorithm is performed through the sequential procedure defined in Box 1. With the internal loop 2, the results gradually change, from the trial solution to the original one, by solving a sequence of closely related optimization problems. Each problem of this sequence is defined by a modified target tensor, which is adjusted till reaching the original target value $\hat{C}$.

Following the idea introduced by Amstutz and Andrä [14], the external loop 1 handles a sequence of finite element mesh refinements. The initial loop starts with a rather coarse mesh. After convergence, the mesh is refined and the level set function is projected onto the new mesh. This process is repeated until reaching a given accuracy. According to Amstutz and Andrä [14], the objective pursued with this mesh mapping strategy is to improve the algorithm response respect to local minimum. In the present version, they are tested with the coarser meshes, by fixing the step length to $\xi = 0.1$ in equation (49). Once the finest mesh is solved, the activation of the line search provides a more controlled approach to a specific local minimum.

References

[1] X. Zheng, H. Lee, T.H. Weisgraber, M. Shusteff, J. DeOtte, E. B Duoss, J.D. Kuntz, M.M. Biener, Q. Ge, J.A. Jackson, et al. Ultralight, ultrastiff mechanical metamaterials. *Science*, 344(6190):1373–1377, 2014.

[2] M. Kadic, T. Bückmann, R. Schittny, and M. Wegener. Metamaterials beyond electromagnetism. *Reports on Progress in Physics*, 76(12):126501, 2013.

[3] S. Narayana and Y. Sato. Heat flux manipulation with engineered thermal materials. *Physical Review Letters*, 108(21):214303, 2012.

[4] A.N. Norris. Acoustic cloaking theory. In *Proceedings of the Royal Society of London A: Mathematical, Physical and Engineering Sciences*, volume 464, pages 2411–2434, 2008.

[5] J.B. Pendry, D. Schurig, and D.R. Smith. Controlling electromagnetic fields. *science*, 312(5781):1780–1782, 2006.

[6] Y. Cheng, F. Yang, J.Y. Xu, and X.J. Liu. A multilayer structured acoustic cloak with homogeneous isotropic materials. *Applied Physics Letters*, 92(15): 151913, 2008.

[7] G.W. Milton and A.V. Cherkaev. Which elasticity tensors are realizable? *Journal of engineering materials and technology*, 117(4):483–493, 1995.

[8] C.N. Layman, C.J. Naify, T.P. Martin, D.C. Calvo, and G.J. Orris. Highly anisotropic elements for acoustic pentamode applications. *Physical review letters*, 111(2):024302, 2013.

[9] M. Kadic, T. Bückmann, R. Schittny, P. Gumbsch, and M. Wegener. Pentamode metamaterials with independently tailored bulk modulus and mass density. *Physical Review Applied*, 2(5):054007, 2014.

[10] Martin Philip Bendsøe and Noboru Kikuchi. Generating optimal topologies in structural design using a homogenization method. *Computer methods in applied mechanics and engineering*, 71(2):197–224, 1988.

[11] Martin Philip Bendsoe and Ole Sigmund. *Topology optimization: theory, methods, and applications*. Springer Science & Business Media, 2013.

[12] O. Sigmund and K. Maute. Topology optimization approaches. *Structural and Multidisciplinary Optimization*, 48(6):1031–1055, 2013.

[13] M. Osanov and J.K. Guest. Topology optimization for architected materials design. *Annual Review of Materials Science*, 46:211–233, 2016.

[14] S. Amstutz and H. Andrä. A new algorithm for topology optimization using a level-set method. *Journal of Computational Physics*, 216(2):573–588, 2006.

[15] S. Amstutz, S.M. Giusti, A.A. Novotny, and E.A. de Souza Neto. Topological derivative for multi-scale linear elasticity models applied to the synthesis of microstructures. *International Journal for Numerical Methods in Engineering*, 84(6):733–756, 2010.

[16] S Amstutz, AA Novotny, and EA de Souza Neto. Topological derivative-based topology optimization of structures subject to drucker–prager stress constraints. *Computer Methods in Applied Mechanics and Engineering*, 233:123–136, 2012.

[17] R Amigo, SM Giusti, AA Novotny, ECN Silva, and J Sokolowski. Optimum design of flextensional piezoelectric actuators into two spatial dimensions. *SIAM Journal on Control and Optimization*, 54(2):760–789, 2016.

[18] A.A. Novotny and J. Sokołowski. *Topological derivatives in shape optimization.* Springer Science & Business Media, 2012.

[19] İ. Özdemir. Topological derivative based optimization of 3d porous elastic microstructures. *Computational Materials Science*, 81:319–325, 2014.

[20] N.H. Gokhale, J.L. Cipolla, and A.N. Norris. Special transformations for pentamode acoustic cloaking. *The Journal of the Acoustical Society of America*, 132(4):2932–2941, 2012.

[21] G.W. Milton. The theory of composites. *The Theory of Composites, by Graeme W. Milton, pp. 748. ISBN 0521781256. Cambridge, UK: Cambridge University Press, May 2002.*, page 748, 2002.

[22] N. Auffray and P. Ropars. Invariant-based reconstruction of bidimensional elasticity tensors. *International Journal of Solids and Structures*, 87:183–193, 2016.

[23] T.C. Ting. *Anisotropic elasticity: theory and applications.* Number 45. Oxford University Press on Demand, 1996.

[24] L.D. Landau and E.M. Lifshitz. *Course of Theoretical Physics Vol 7: Theory and Elasticity.* Pergamon Press, 1959.

[25] O. Sigmund. A new class of extremal composites. *Journal of the Mechanics and Physics of Solids*, 48(2):397–428, 2000.

[26] L.J. Walpole. On bounds for the overall elastic moduli of inhomogeneous systemsi. *Journal of the Mechanics and Physics of Solids*, 14(3):151–162, 1966.

[27] A.V. Cherkaev and L.V. Gibiansky. Coupled estimates for the bulk and shear moduli of a two-dimensional isotropic elastic composite. *Journal of the Mechanics and Physics of Solids*, 41(5):937–980, 1993.

[28] A Ferrer, J Oliver, JC Cante, and O Lloberas-Valls. Vademecum-based approach to multi-scale topological material design. *Advanced Modeling and Simulation in Engineering Sciences*, 3(1):23, 2016.

[29] S.M. Giusti, A. Ferrer, and J. Oliver. Topological sensitivity analysis in heterogeneous anisotropic elasticity problem. theoretical and computational aspects. *Computer Methods in Applied Mechanics and Engineering*, 311:134–150, 2016.

[30] M.F. Ashby. *Materials selection in mechanical design*. Elsevier, Butterworth-Heinemann, 3rd. edition, 2005.

[31] J.M. Podestá, A.E. Huespe, C. Méndez, and V. Fachinotti. Diseño computacional de metamateriales ultrarígidos y ultralivianos. *Mecánica Computacional*, 35, 2016.

[32] B. Banerjee. *An introduction to metamaterials and waves in composites*. CRC Press, 2011.

[33] R.W. Ogden. *Non-linear elastic deformations*. Courier Corporation, 1997.

[34] E.A. de Souza Neto and R.A. Feijóo. Variational foundation on multi-scale constitutive models of solids: small and large strain kinematical formulation. *LNCC Research & Development Report No 16*, 16, 2006.

[35] S.M. Giusti. *Análise de sensibilidade topológica em modelos constitutivos multi-escalas*. PhD thesis, Laboratrio Nacional de Computao Cientfica, LNCC, Brasil, 2009.